

Mott insulating states with competing orders in the triangular lattice Hubbard model

Alexander Wietek,^{1,*} Riccardo Rossi,^{1,2} Fedor Šimkovic IV,^{3,4} Marcel Klett,⁵ Philipp Hansmann,⁶
Michel Ferrero,^{3,4} E. Miles Stoudenmire,¹ Thomas Schäfer,⁵ and Antoine Georges^{4,1,3,7}

¹*Center for Computational Quantum Physics, Flatiron Institute, 162 Fifth Avenue, New York, NY 10010, USA*

²*Institute of Physics, École Polytechnique Fédérale de Lausanne (EPFL), CH-1015 Lausanne, Switzerland*

³*CPHT, CNRS, École Polytechnique, IP Paris, F-91128 Palaiseau, France*

⁴*Collège de France, 11 place Marcelin Berthelot, 75005 Paris, France*

⁵*Max-Planck-Institut für Festkörperforschung, Heisenbergstraße 1, 70569 Stuttgart, Germany*

⁶*Department of Physics, University of Erlangen-Nürnberg, 91058, Erlangen, Germany*

⁷*DQMP, Université de Genève, 24 quai Ernest Ansermet, CH-1211 Genève, Suisse*

(Dated: October 20, 2021)

The physics of the triangular lattice Hubbard model exhibits a rich phenomenology, ranging from a metal-insulator transition, intriguing thermodynamic behavior, and a putative spin liquid phase at intermediate coupling, ultimately becoming a magnetic insulator at strong coupling. In this multi-method study, we combine a finite-temperature tensor network method, minimally entangled thermal typical states (METTS), with two Green function-based methods, connected-determinant diagrammatic Monte Carlo (DiagMC) and cellular dynamical mean-field theory (CDMFT), to establish several aspects of this model. We elucidate the evolution from the metallic to the insulating regime from the complementary perspectives brought by these different methods. We compute the full thermodynamics of the model on a width-4 cylinder using METTS in the intermediate to strong coupling regime. We find that the insulating state hosts a large entropy at intermediate temperatures, which increases with the strength of the coupling. Correspondingly, and consistently with a thermodynamic Maxwell relation, the double occupancy has a minimum as a function of temperature which is the manifestation of the Pomeranchuk effect of increased localisation upon heating. The intermediate coupling regime is found to exhibit both pronounced chiral as well as stripy antiferromagnetic spin correlations. We propose a scenario in which time-reversal symmetry broken states compete with stripy-spin states at lowest temperatures.

I. INTRODUCTION

The interplay between strong electronic interactions and geometric frustration gives rise to a plethora of intriguing physical phenomena. It also raises fundamental questions that are still largely open, such as how insulating spin liquids transition into a metallic or superconducting phase upon reducing the interaction strength or introducing doped charge carriers.

Several classes of experimental platforms are available in which these questions can be explored. The most recent one is the rapidly developing field of twisted moiré heterostructures of two-dimensional materials, such as graphene [1–3] or transition-metal dichalcogenides [4, 5]. Recent work has demonstrated that these heterostructures provide a versatile platform for quantum materials design in which a broad range of lattice and band structures can be engineered [6, 7]. A triangular lattice structure, which is the focus of the present paper, can be realized in this context for B moiré superlattices [8, 9], twisted WSe₂ double bilayers [10] as well as twisted bilayer Boron Nitride [11, 12]. The observation of a Mott insulating state in e.g. the WSe₂/WS₂ moiré superlattice system [8] provides direct experimental evidence of the importance of strong electronic correlations in these materials. We also note that the triangular superlat-

tice dichalcogenide 1T-TaS₂ has been proposed to host a spin-liquid state [13–16].

Besides moiré materials, strong electronic correlations in the context of (anisotropic) triangular lattice structures are also directly relevant to the two-dimensional molecular materials of the κ -ET family [17]. This class of materials has been the subject of intense experimental research and displays a diversity of remarkable phenomena (for reviews, see e.g. [18, 19]). Among those are Mott insulating phases with either magnetic long-range order or spin liquid behavior as in e.g. κ -(ET)₂Cu₂(CN)₃, a pressure-induced metal-insulator transition (MIT). Several experiments found evidence of first-order phase transitions at finite-temperature up to a proposed critical temperature of ~ 20 K [20, 21]. Moreover, superconductivity with a critical temperature reaching ~ 14 K has been found. [21–31]. Finally, transition metal oxides such as the layered superconductor Li_xNbO₂ also form triangular lattices, with structural similarities to some of the dichalcogenides [32–34].

While the Hubbard model [35–38] on the triangular lattice is directly relevant to this wide variety of materials, it is also a paradigmatic model of strongly correlated electrons subject to geometric frustration and has therefore been subject to intense computational and theoretical research [39, 40]. However, due to the high complexity of the problem, only a partial understanding of its physics has been reached. The model is defined by the Hamilto-

* awietek@flatironinstitute.org

nian:

$$\hat{H} = -t \sum_{\langle i,j \rangle, \sigma} \left(\hat{c}_{i\sigma}^\dagger \hat{c}_{j\sigma} + \hat{c}_{j\sigma}^\dagger \hat{c}_{i\sigma} \right) + U \sum_i \hat{n}_{i\uparrow} \hat{n}_{i\downarrow}, \quad (1)$$

where $\hat{c}_{i\sigma}^\dagger, \hat{c}_{i\sigma}$ denote the fermionic creation and annihilation operators on site i with fermion spin σ , $\hat{n}_{i\sigma} = \hat{c}_{i\sigma}^\dagger \hat{c}_{i\sigma}$, and $\langle i, j \rangle$ denotes summation over nearest-neighbor bonds of the triangular lattice.

At half-filling ($\langle \hat{n}_{i\uparrow} + \hat{n}_{i\downarrow} \rangle = 1$) the model has a metallic phase for small U/t , while it is an insulator with long-range magnetic order in the large U/t limit for $T = 0$. At finite temperatures true long-range magnetic order is prohibited in two dimensions by the Mermin-Wagner theorem [41, 42]. It has been suggested early on that an intermediate insulating phase without magnetic long-range order exists between these two phases, at intermediate U/t [43][44]. The existence of this intermediate phase has been corroborated by several different computational methods [45–52]. Recent density matrix renormalization group (DMRG) studies showed strong evidence that the intermediate phase ground state realizes a gapped chiral spin liquid (CSL) [52–54]. This elusive state of matter has been proposed in the late 1980s [55, 56] and in the last years has been found to be stabilized in several frustrated spin systems [57–63], including extended triangular lattice spin-1/2 Heisenberg models [64, 65]. The demonstration of the emergence of topological superconductivity upon hole-doping the triangular lattice CSL [66] (see also [67]) constitutes an exciting prospect for the physics of the moiré materials and organic superconductors. Other previous suggestions on the nature of the intermediate phase include a Gutzwiller projected Fermi sea [68–70] and other forms of gapless spin liquids [71–73]. However, the existence of the intermediate CSL phase is also challenged by earlier DMRG results [74] as well as recent variational Monte Carlo studies, suggesting the absence of a spin liquid phase close to the metal-insulator transition [75, 76]. Other recent DMRG results on width 3 cylinders have suggested a gapless spin liquid being realized in the intermediate phase [77].

Computational methods for studying quantum many-body systems rely on diverse concepts and usually involve approximations whose validity has to be subject to critical evaluation. In the context of the Hubbard model, direct comparisons and benchmark studies involving multiple methods have proved successful in establishing the physics in the strongly correlated [78–80] and intermediate coupling [81] regimes beyond the uncertainties associated with the limitations of one particular method (see also a recent study on the kagome lattice [82]). This multi-method approach is currently playing a crucial role in the field and accelerates further theoretical and computational developments.

In this article, we combine conceptually different methods to investigate the physics of the half-filled triangular lattice Hubbard model at finite temperature. For some physical observables, the results from these different methods can be directly compared, but each

method also comes with physical observables that it can more naturally address. Such a ‘multi-method, multi-messenger’ approach [81] therefore allows us to investigate the physics of this complex model from different perspectives.

On the one hand, we employ the minimally entangled thermal typical state method (METTS) [83, 84] which is an extension of DMRG to finite temperature. On the other hand, we use two Green function based techniques, the diagrammatic Monte Carlo method (DiagMC [85]) in its connected determinant version [86–90], dynamical mean-field theory (DMFT [91–94]) and a cluster extension [95] thereof: cellular DMFT (CDMFT) [96, 97] in its center-focused formulation [98]. Such a ‘handshake’ between wave-function based and Green function based methods is a notable advance which opens new perspectives for the study of quantum many-body problems at finite temperature.

Each of these methods has strengths and limitations which we now briefly describe. As a matrix-product state technique METTS can be applied with high precision on cylindrical geometries of finite circumference, as demonstrated recently by some of the authors in the case of the hole-doped square lattice Hubbard model [99], where a detailed description of the implementation of the method can be found. In this manuscript we mostly focus on a particular cylindrical geometry of circumference 4, called the YC4 geometry shown in Fig. 7. Selected results on the XC4 and YC3 geometries (see e.g. [52]) are also presented for comparison. Since we demonstrate convergence of our results in the maximal bond dimension D_{\max} (Appendix A), the main limitation is in the finite transverse size.

As the triangular-lattice Hubbard model is afflicted by the fermionic sign problem, we cannot use traditional Quantum Monte Carlo techniques [100]. Diagrammatic Monte Carlo can work directly in the thermodynamic limit and is therefore immune from the sign problem, while being numerically exact: it is possible to compute quantities with arbitrary precision given enough computational time, and the convergence can be checked by comparing results from different expansion orders. Reaching the strong-coupling regime can, however, be hindered by the increased difficulty of resumming the perturbative series beyond their radius of convergence [87], and many orders must be computed, which in itself can present computational challenges. In this work, using the recent computational advances of the connected-determinant version [86], we are able to compute up to 10 orders of the perturbative expansion at fixed density; this is achieved [101] by renormalizing the chemical potential in the spirit of [89]. Thanks to the high orders reached, we manage to get converged results with controlled errorbars at temperatures $T/t = 0.1$ and up to $U/t = 10$.

CDMFT also works directly in the thermodynamic limit for the lattice, but it retains only a finite number of real-space components of the self-energy organized

according to spatial locality and approximated by their value on a (self-consistent) cluster of finite size N_c . The method is controlled in the sense that it converges to the exact solution in the limit $N_c \rightarrow \infty$, but in practice, this convergence can only be reached in specific parameter regimes. Here, CDMFT is used in a twofold way: (i) as an approximation with $N_c = 7$ restricted to the paramagnetic (PM) phase [CDMFT-7 (PM)] and (ii) as an approximation with $N_c = 4$ (CDMFT-4) allowing for magnetic ordering. Unless noted otherwise the label “CDMFT” denotes results from the first variant. In either case on-site and nearest-neighbor components of the self-energy are taken into account, besides all temporal (quantum) correlations already present in single-site DMFT.

This article is organized as follows. We discuss the transition from a metallic state at weak-coupling to an insulating state at strong coupling in Sec. II. There, we perform a critical comparison between our numerical methods and propose that, in the accessible range of temperatures, a smooth crossover between these states is found rather than a first-order phase transition. In Sec. III we discuss the locality of the electronic self-energy by comparing results from CDMFT and DiagMC. In Sec. IV we investigate the basic thermodynamic properties of the system and firmly establish an order-by-disorder effect, where increasing temperature decreases the double occupancy. We relate this effect to an increase in entropy upon increasing the interaction strength via a Maxwell relation. Sec. V discusses competing (magnetic) orders as a function of temperature and interaction strength. In particular, we investigate magnetic structure factors and the chiral susceptibility to propose a scenario where chiral and stripy antiferromagnetic spin correlations coexist at low temperatures. Finally, we summarize and discuss our findings in Sec. VI.

II. METAL-INSULATOR CROSSOVER

We begin by investigating the evolution from a metallic state at weak coupling to a Mott insulating state at strong coupling. At high enough temperature, this is a crossover. Whether it remains a crossover down to lowest temperatures or whether a phase transition also exists at low but finite temperature is discussed at the end of this section.

In order to identify this crossover, we consider two complementary observables, which are accessible within the CDMFT and METTS frameworks respectively. The first one is the zero-frequency value of the local (on-site) electronic spectral function:

$$A_c(\omega = 0) = -\frac{1}{\pi} \text{Im} G_c(i\omega_n \rightarrow i0^+). \quad (2)$$

This quantity is evaluated by considering the central site of the cluster within the center-focused CDMFT method (see App. D and [98]) — hence the subscript in A_c . The

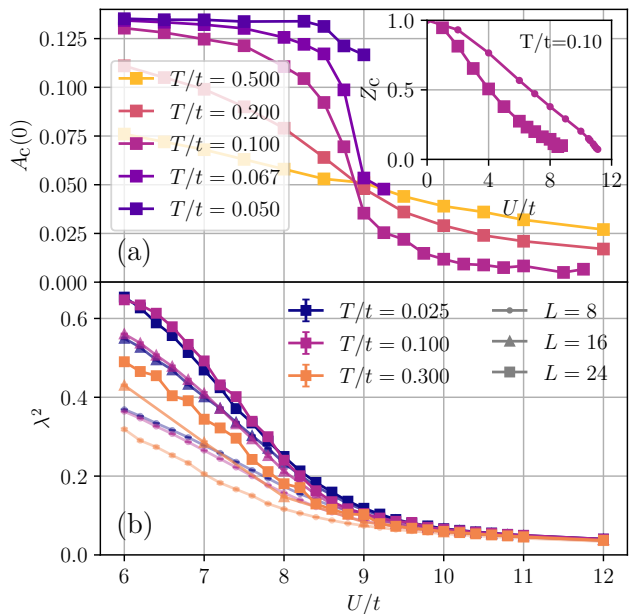


FIG. 1. Metal-Insulator crossover at finite-temperature from CDMFT and METTS. (a) Spectral weight at the Fermi level from CDMFT. The inset shows the quasiparticle renormalization factor for the central site in CDMFT (squares) as well as for PM-restricted DMFT (dots). A drop of the spectral weight at the Fermi level is observed. (b) Normalized localization length as a function of temperature and system size as obtained from METTS on the YC4 cylinder. Simulations have been performed with maximal bond dimension $D_{\max} = 4000$. The normalized localization length attains a finite value in the insulating regime and increases in the linear system size L in the metallic regime, where higher temperatures decrease the localization length.

extrapolation to zero frequency is obtained from a fit of the Matsubara frequency Green’s function $G(i\omega_n)$. We have also calculated within CDMFT the local and nearest-neighbor components of the self-energy and can extract the low-frequency slope:

$$Z_c = \left[1 - \left. \frac{\partial \Sigma_c}{\partial \omega} \right|_{\omega \rightarrow 0} \right]^{-1}, \quad (3)$$

which is also a good indicator of the MIT. The non-local components of the self-energy are found to be quite small for weak to intermediate U/t (see Sec. III for more details), hence Z_c is a reasonable approximation in this regime to the spectral weight of quasiparticles. $A_c(0)$ is plotted in Fig. 1(a) as a function of U/t for several values of temperature, along with Z_c at $T/t = 0.1$ (inset). We see that for each value of T , $A_c(0)$ undergoes a marked drop as U/t is increased, signalling a crossover from a metal with a large value of the zero-frequency spectral density to an insulator with a small one (but as expected still finite at non-zero T). Being a crossover there is a certain arbitrariness in defining its location precisely but it is apparent that, at the lowest temperatures, it occurs for

$8 \lesssim U/t \lesssim 9$. Correspondingly, Z_c drops rapidly as U/t is increased. At still larger values of U/t , the CDMFT self-energy has the characteristic divergent low-frequency behavior of an insulator, see Fig. 17 in Appendix D. Importantly, we see that $A_c(0)$ increases upon cooling for $U/t \lesssim 9$, while it decreases upon cooling for $U/t \gtrsim 9$, which are the expected behaviors in a metallic and an insulating regime, respectively. We note that for small temperatures and large interactions the CDMFT calculation becomes increasingly difficult due to the fermionic sign problem.

The evolution from a metallic state to an insulating state can also be characterized by the localization of electrons [102, 103]. An appropriate measure of localization is given by the localization length λ , which on open boundary conditions as employed by METTS is defined as [104–106],

$$\lambda^2 = \frac{1}{N} \left(\langle X^2 \rangle - \langle X \rangle^2 \right). \quad (4)$$

Here, $X = \sum_i r_i n_i$ denotes the position operator, where r_i denote the coordinates of the lattice, n_i the local density operators, and N the total number of sites.

At zero temperature, the localization length λ is directly related to the real part of the conductivity $\sigma(\omega)$ by [107]

$$\lambda^2 = \frac{\hbar}{\pi e^2 n} \int_0^\infty \frac{d\omega}{\omega} \text{Re } \sigma(\omega), \quad (T = 0) \quad (5)$$

where e denotes the electron charge and n the average density. The integral on the right-hand side, also referred to as Souza-Wilkens-Martin integral [104, 106, 107], diverges in the metallic regime and attains a finite value in the insulating regime for $N \rightarrow \infty$. The behavior of λ^2 for temperatures $T/t = 0.025, 0.100, 0.300$ and YC4 cylinder lengths $L = 8, 16, 24$ computed by METTS is shown in Fig. 1(b). The metallic and insulating regimes can be coarsely distinguished by the behavior of λ^2 . Whereas in the insulating regime, λ^2 is almost constant as a function of the cylinder length L and temperature, it increases with L in the metallic regime. We also observe that at higher temperature, such as $T/t = 0.300$ in Fig. 1(b), the localization length decreases, indicating increased localization of the system.

Furthermore, we study the behavior of the charge structure factor given by,

$$S_c(\mathbf{k}) = \frac{1}{N} \sum_{l,m=1}^N e^{i\mathbf{k}\cdot(\mathbf{r}_l - \mathbf{r}_m)} \langle (n_l - \langle n_l \rangle)(n_m - \langle n_m \rangle) \rangle, \quad (6)$$

where n_l denotes the local density at site l . When using METTS we are working in the canonical ensemble with zero global charge fluctuation, which implies $S_c(0) = 0$ at any temperature. The behavior of $S_c(\mathbf{k})$ around $\mathbf{k} = 0$ is indicative of metallic or insulating behavior. While a metallic state at $T = 0$ is characterized by a linear charge

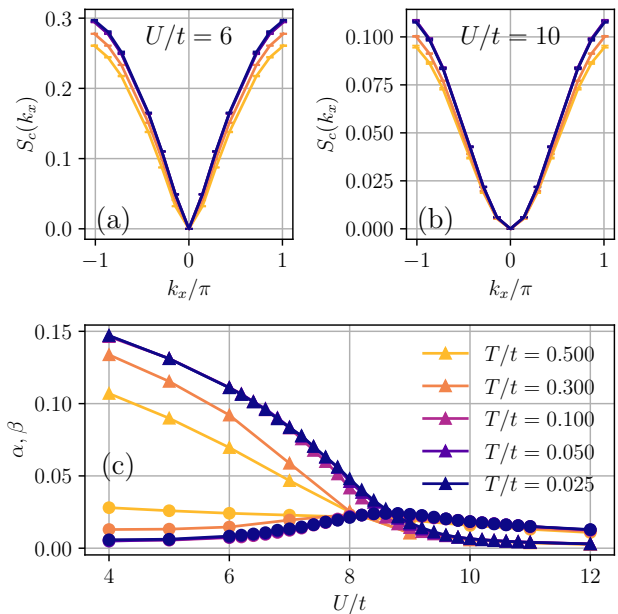


FIG. 2. Static charge structure factor $S_c(\mathbf{k})$ for $k_y = 0$ at various temperatures (see legend in (c)) on the 16×4 YC4 cylinder from METTS with maximal bond dimension $D_{\max} = 4000$. (a) In the metallic regime at $U/t = 6$, the density structure factor behaves as $S_c(k_x) \approx \alpha|k_x|$. (b) In the insulating regime at $U/t = 10$ we observe $S_c(k_x) \approx \beta k_x^2$. (c) Optimal fit parameters α, β for the ansatz $S_c(k_x) = \alpha|k_x| + \beta k_x^2$ of $S_c(k_x)$ close to $k_x = 0$. α (resp. β) is shown as triangles (resp. circles). The crossover interaction strength U_c/t can be defined by the intersection of α and β . We observe U_c/t shifting towards weaker interactions at higher temperatures.

dispersion [108–111],

$$S_c(\mathbf{k}) \approx \alpha|k_x|, \quad (7)$$

an insulating state exhibits a quadratic dispersion,

$$S_c(\mathbf{k}) \approx \beta k_x^2. \quad (8)$$

The behavior of the charge structure factor on the 16×4 YC4 cylinder from METTS at various temperatures in Fig. 2. We compare between the metallic regime at $U/t = 6$ in (a) and the insulating regime at $U/t = 10$ in (b). The two regimes clearly exhibit the expected linear (resp. quadratic) behavior close to \mathbf{k} . We observe a rather mild temperature dependence. To quantify this behavior, we make the following ansatz close to $k_x = 0$,

$$\tilde{S}_c(\mathbf{k}) = \alpha|k_x| + \beta k_x^2. \quad (9)$$

The value of α (resp. β) can be interpreted as a metallic (resp. insulating) weight. We fit this ansatz to the numerical data shown in Fig. 2(a,b) for the seven k -points closest to the origin. Results for a range from $U/t = 4$ to $U/t = 12$ are shown in Fig. 2(c). At low U/t in the metallic regime, we observe that increasing temperature

decreases the metallic weight α while increasing the insulating weight. In the insulating regime, we observe only a weak temperature dependence of α and β . We can define a crossover interaction strength U_c/t by the intersection of $\alpha(U)$ and $\beta(U)$. We observe that U_c/t shifts towards weaker interaction strengths when increasing temperatures. From this we estimate $U_c/t \approx 8.7$ at $T/t = 0.025$, $U_c/t \approx 8.5$ at $T/t = 0.100$, and $U_c/t \approx 8.0$ at $T/t = 0.500$. This also implies that, for a fixed U/t in that range, the system undergoes increased localisation upon heating.

To further study the metal to insulator crossover we investigate the potential energy,

$$E_{\text{pot}} = U \sum_i \langle \hat{n}_{i\uparrow} \hat{n}_{i\downarrow} \rangle, \quad (10)$$

and the kinetic energy,

$$E_{\text{kin}} = -t \sum_{\langle i,j \rangle, \sigma} \langle \hat{c}_{i\sigma}^\dagger \hat{c}_{j\sigma} + \hat{c}_{j\sigma}^\dagger \hat{c}_{i\sigma} \rangle. \quad (11)$$

Since these quantities are accessible with all our methods, we show a direct comparison in Fig. 3(a,b) to assess the effects of finite cluster size in CDMFT and finite cylinder size in METTS. We focus on a temperature of $T/t = 0.1$, for which we perform numerically-exact simulations with DiagMC up to $U/t = 10.5$, which are used as benchmark. Remarkably, results from all methods agree within error bars up to an interaction strength of $U/t = 8$. Beyond this point, we still observe that the potential energy from METTS compares well with CDMFT [with $N_c = 7$ and restricted to its paramagnetic solution, CDMFT-7 (PM)] up to the strong coupling regime $U/t = 12$. A key difference between METTS and CDMFT is seen in the kinetic energy, which is lower for METTS in the strong coupling regime. We also note that the CDMFT kinetic energy exhibits a slope discontinuity around $U/t \sim 9$ which is not observed by METTS: as discussed below, this is due to the fact that a finite-temperature metal-insulator transition is found within CDMFT (as well as DMFT) when constrained to non-magnetic solutions. Nonetheless, the data from CDMFT overall agrees more closely with METTS than the data from single-site DMFT.

Above $T/t \simeq 0.1$, all methods agree that the passage from the metal to the insulator is a smooth crossover [112]. Furthermore, it is clear from previous work [45–48, 52, 53, 113], that at $T = 0$ a metal-insulator phase transition (MIT) takes place. We now discuss whether our data allow us to settle whether a sharp MIT also exists at low but finite temperature or whether a smooth crossover applies for any non-zero temperature.

Let us first recall what the situation is in the single-site DMFT approximation. When solving the DMFT equations constrained to solutions without long-range magnetic order, one indeed finds that a first-order MIT develops for $T < T_c^{\text{DMFT}} \simeq 0.1t$ ($U_c^{\text{DMFT}}/t \simeq 11$) as previously demonstrated by several authors and also shown in Fig. 13 of Appendix C. Since there is no symmetry

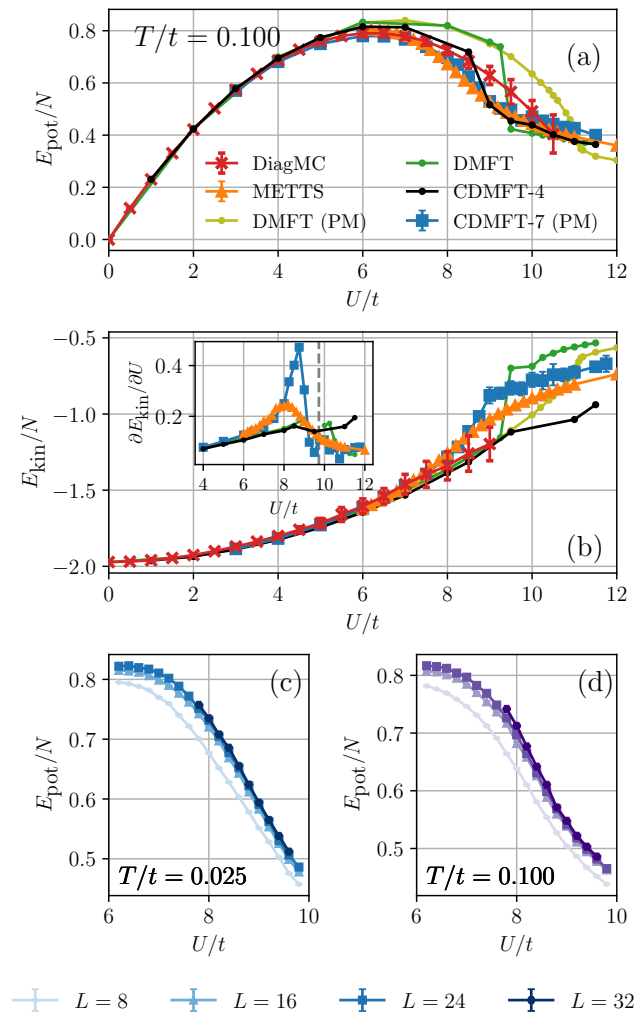


FIG. 3. Comparison of energies from different computational methods at $T/t = 0.1$. METTS results are obtained on a 16×4 YC4 cylinder with $D_{\text{max}} = 4000$, cluster DMFT is performed on a 7-site cluster [restricted to its paramagnetic solution, CDMFT-7 (PM)] and on a 4-site cluster (allowing for spin-symmetry breaking, CDMFT-4), while DiagMC is numerically-exact within the estimated errorbar. (a) Potential energy E_{pot} . METTS and cluster-DMFT agree with the DiagMC results up to $U/t \approx 7.5$. Beyond this point we find excellent agreements between cluster DMFT and METTS. (b) Kinetic energy E_{pot} . We observe good agreement between all methods up to $U/t = 8$. The inset shows the derivative of the kinetic energy w.r.t. the coupling strength U . (c,d) The potential energy density from METTS as a function of cylinder length L at temperatures $T/t = 0.025$ and $T/t = 0.100$. We observe a smooth dependence on the coupling strength and for both temperatures upon increasing the system size.

distinction at finite temperature between a metal and an insulator with no broken symmetries, a first-order transition line ending at a second-order critical endpoint (U_c, T_c) (analogous to a liquid-gas transition) is a priori possible. This is what happens in DMFT [93, 114–

[122], as well as in cluster extensions of DMFT [123–128] when restricted to non-magnetic solutions. This transition is the reason for the cusp in the kinetic energy found with these methods, as apparent on Fig. 3(b) around $U_c^{\text{CDMFT}}/t \simeq 9$. However it should be emphasized that, when allowing for spin and translational symmetry breaking, the single-site DMFT approximation yields a solution with 120° Néel ordering for $U/t \gtrsim 9.5$ [113] (see Appendix C): this is the true minimum of the free-energy in the DMFT approximation, hence overshadowing the first-order non-magnetic MIT. Incidentally, we note that the magnetically ordered DMFT solution yields a rather good approximation to both the kinetic and potential energy (Fig. 3).

Analogously to the DMFT case, we also computed the energetics within CDMFT on a $N_c = 4$ site cluster, however now allowing for magnetic symmetry breaking (CDMFT-4). The order sets in at similar interaction strengths as in the case of DMFT. Due to the smaller size of the cluster, and therefore the shorter non-local correlations that are included in the calculation, deviations from CDMFT-7 (PM) appear for the potential energy in the paramagnetic regime at intermediate coupling. At larger interaction strengths, when CDMFT-4 has ordered with a 120° Néel pattern, the potential energy acquires similar values to both METTS and CDMFT-7 (PM). In case of the kinetic energy, we observe deviations also in the ordered phase. They might root in the fact that the cluster geometries differ between CDMFT-7 (PM) and CDMFT-4 (for further details we refer to App. D). We note that calculations in the symmetry-broken phase for a $N_c = 7$ site cluster are not feasible at the moment due to the fermionic sign problem.

Of course, the magnetic solution at non-zero temperature is an artefact of the mean-field approximation inherent to DMFT, and one may argue that because fluctuations and Mermin-Wagner theorem actually prevent ordering, the existence of a finite- T MIT in paramagnetic DMFT/CDMFT is a hint that a similar phenomenon might take place in our model. On a qualitative level, frustration appears as a favorable factor by further suppressing ordering. The ET-organic materials with an (anisotropic) triangular structure do display such a transition experimentally [19].

Our METTS and DiagMC results do not provide evidence for such a first-order MIT or liquid-gas critical endpoint at finite temperature. In the range of temperatures that we could investigate, the kinetic and potential energy displayed in Fig. 3 do not appear to have a singularity as a function of U/t . However, we acknowledge that limitations of our computational methods prevent us to reach a definitive conclusion about this issue. Our METTS results yield a smooth crossover between the metallic and the insulating regime for temperatures down to $T/t = 0.025$. This is expected, since our simulations are performed on a finite system. Hence, observables will depend smoothly on the model parameters. We have, however, investigated the possibility of a discontinuity,

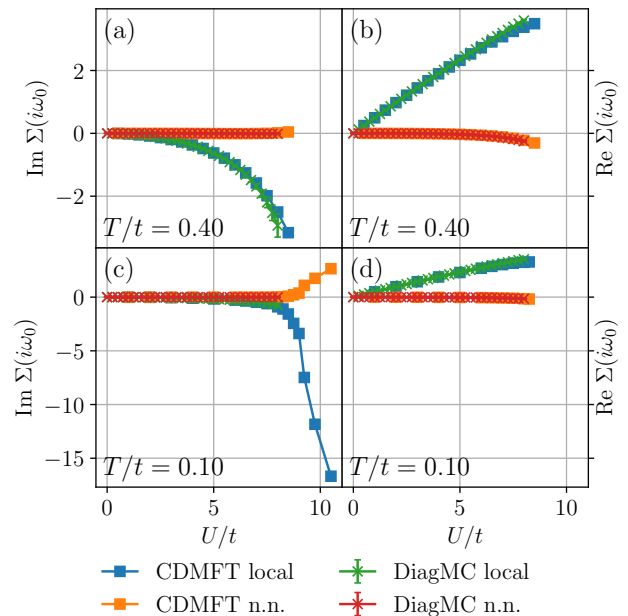


FIG. 4. Imaginary (left panels) and real (right panels) parts of the local (blue) and nearest neighbor (orange) self-energy at its lowest Matsubara frequency calculated by DiagMC (crosses) and CDMFT (squares) as a function of U/t for two different temperatures $T/t = 0.4$ (upper panels) and $T/t = 0.1$ (lower panels). A substantial increase of non-local correlations is observed at low temperatures, however, at interactions ($U/t \approx 9.25$) larger than the one of increased local correlations ($U/t \approx 8$).

indicative of a first-order phase transition, developing as a function of the length of the YC4 cylinder. Our results are shown for temperatures $T/t = 0.025$ in Fig. 3(c) and for $T/t = 0.100$ in Fig. 3(d). The smooth behavior at all system sizes does not exhibit any tendency to develop a discontinuity for $L \rightarrow \infty$. However, it is possible that the chosen cluster geometry or the finite precision we achieve conceal potential singularities developing in the infinite-volume limit. The data points shown in Fig. 1 are spaced by $\Delta U = 0.2t$ where the maximal absolute statistical error is of size $\varepsilon \approx 5 \cdot 10^{-3}$. The DiagMC results, while dealing with the infinite system, are limited in the present work to $T/t \gtrsim 0.1$ and $U/t \lesssim 10$. This is largely due to difficulties in computing enough expansion coefficients with small enough error bars to allow for controlled resummations of the perturbative series beyond the aforementioned values of U .

III. (NON-)LOCALITY OF CORRELATIONS: SELF-ENERGIES

Although the electronic Coulomb interaction is modeled as a purely local repulsion in the Hubbard model in Eq. (1), the correlations it generates can be non-local. To assess in which part of the phase diagram non-local

correlations become sizable in comparison to local ones, we calculate the local and nearest-neighbor (n.n.) self-energy in DiagMC and CDMFT in real space on the Matsubara axis. Fig. 4 displays the self-energy at the first Matsubara frequency $\Sigma(i\omega_0 = i\pi T)$ calculated by DiagMC (crosses) and CDMFT (squares) for two different temperatures (left panels: imaginary part, right panels: real part). The results of the calculations from both methods agree within error bars for both local and n.n. components.

At high $T/t=0.40$ the correlations are mostly local and continuously increase from small to large U . However, there is an onset of non-locality already visible in the increase of the n.n. component at the largest interactions shown. The non-local correlations remain very small at lower $T/t=0.10$ (close to the critical temperature of the MIT in CDMFT), until quite close to $U/t \approx 9.25$ at which the MIT takes place in CDMFT. Hence, through most of the metallic regime except close to the MIT, the self-energy in this temperature range is local to a good approximation in this frustrated system.

Upon entering the insulating regime, non-local correlations continuously increase. These non-local correlations signal increasing magnetic fluctuations. The onset of a magnetically ordered phase in DMFT (see App. C) underpins this interpretation. In the true solution of the system, of course, the Mermin-Wagner theorem [41, 42] prohibits magnetic ordering at finite temperature but the corresponding magnetic fluctuations are responsible for the increase of the (non-local) correlations. We note that the effect of magnetic fluctuations beyond DMFT using the dual fermion approximation has been investigated for this model in Refs. [47, 112, 129] and that the implications of non-local effects for transport has been investigated in Ref. [128].

IV. THERMODYNAMICS

We now turn to discussing the thermodynamic properties of the system for a range of interactions from $U/t = 6$ to $U/t = 12$. Figure 5 displays the specific heat C , thermal entropy S , internal energy E , and double occupancy D as a function of temperature. Results for the specific heat,

$$C = \frac{\partial E}{\partial T}, \quad (12)$$

of the 16×4 YC4 cylinder using METTS at various values of U/t are shown in Fig. 5(a). At intermediate and large interaction strengths $U/t = 9, 10, 12$ the specific heat exhibits a large mostly featureless plateau down to temperatures of $T/t \approx 0.1$. For $U/t = 10, 12$ a small peak develops at $T/t \approx 0.05$ before the specific heat tends towards zero at $T = 0$.

For $U/t = 6, 8$ we find a T -linear behavior of C at low temperature, consistent with a metallic phase with gapless excitations. We note that the low- T slope for $U/t = 8$

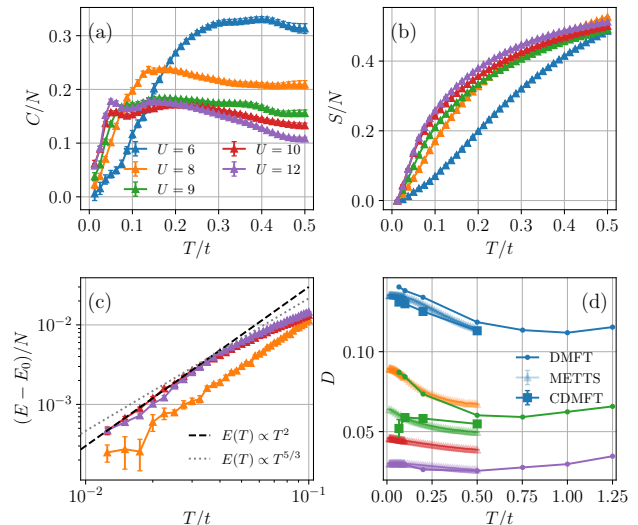


FIG. 5. Thermodynamics of the 16×4 YC4 cylinder from METTS for different values of U/t . We employed a maximal bond dimension $D_{\max} = 3000$ (a) Specific heat C . At $U/t = 9, 10, 12$ we observe a broad continuum at higher temperatures with a small peak at $T/t \approx 0.05$. (b) Thermal entropy S . We observe an increase in entropy when increasing U/t at low temperature. (c) Internal energy E as a function of temperature on a refined grid at lower temperatures. We observe regimes where approximately $E \propto T^2$, which implies T -linear behavior of the specific heat. The black and gray lines indicate $E \propto T^2$ and $E \propto T^{5/3}$ behavior. (d) Double occupancy D . At low temperatures, increasing T/t decreases the double occupancy. This order-by-disorder phenomenon is related to the increase in thermal entropy with U/t by the Maxwell relation $\partial S/\partial U = -\partial D/\partial T$. We compare our data to results from (cluster) DMFT and find the CDMFT data closely matching the METTS results.

is approximately three times larger than that at $U/t = 6$: this is qualitatively consistent with Z_c (inset of Fig. 1) being approximately three times smaller. For a metal in which the self-energy can be approximated as local, the quasiparticle effective mass enhancement which controls the slope of C is related to the quasiparticle weight Z by $m^*/m = 1/Z$. Indeed, as shown in the previous section, the non-local components of the self-energy are small through most of the metallic regime. Our findings for Z_c and the slope of C are thus consistent with quasiparticles developing a rather heavy mass as the insulator is approached. Although this is difficult to ascertain from our data, we find no evidence for a divergence of the effective mass when approaching the MIT however, consistent with the increasing non-locality of the self-energy in this regime (see Sec. III). We also observe that for $U/t = 6$, the specific heat appears to have another quasi-linear regime for $T/t \gtrsim 0.1$.

At larger interaction strengths the low-temperature behavior of C also appears to be linear in T . However, given the few data points in this regime, it is difficult to

discern this behavior from other scenarios. We note that the specific heat of the YC4 cylinder closely resembles the specific heat that has been obtained on smaller clusters using the finite-temperature Lanczos method [130].

We also investigate the thermodynamic entropy,

$$S = \log(\mathcal{Z}) + \frac{E}{T} = S_0 + \int_0^T d\Theta \frac{C(\Theta)}{\Theta}, \quad (13)$$

where \mathcal{Z} denotes the partition function and E the internal energy. S_0 denotes a residual entropy at zero temperature. The entropy is obtained by integrating the specific heat as in Eq. (13) from $T = 0$, where the internal (ground state) energy is computed by DMRG and we assume $S_0 = 0$, i.e. we assume a unique ground state on the finite size cylinder.

Our results from METTS on the YC4 cylinder are shown in Fig. 5(b). Interestingly, we find that the entropy (at fixed T) increases rapidly with increasing interaction strength from the metallic regime at $U/t = 6$ to the insulating regime beyond $U/t = 9$. The increase in thermal entropy as a function of interaction strength has previously also been observed using the finite-temperature Lanczos method on smaller cluster geometries [130]. Naively, one would expect a decrease in entropy when the system is localizing. However, we find the exact opposite behavior, i.e. $\partial S/\partial U > 0$. This behavior is also reflected in the temperature dependence of the double occupancy,

$$D = \frac{1}{N} \sum_{i=1}^N \langle n_{i\uparrow} n_{i\downarrow} \rangle, \quad (14)$$

shown in Fig. 5(d). The Maxwell relation

$$\left. \frac{\partial S}{\partial U} \right|_T = - \left. \frac{\partial D}{\partial T} \right|_U \quad (15)$$

relates the increase in entropy as function of U to a decrease in double occupancy as a function of T . Indeed, as shown on Fig. 5(d), we observe a decrease of D at low- T upon heating, for all displayed values of U/t up to a temperature $T/t \approx 0.5$ at which the double occupancy has a minimum. On this figure, our METTS results are also compared to (C)DMFT which confirms our finding.

This phenomenon is analogous to the Pomeranchuk effect in liquid Helium 3 [131]. When the entropy of the insulating state is larger than that of the metal, increasing temperature indeed leads to increased localisation since this yields a gain in free-energy. To the best of our knowledge, this behavior was first predicted for the Hubbard model on the basis of DMFT studies [132] (see also [114, 115, 129, 133, 134]). It has been proposed [135] and experimentally realized [136] as a cooling scheme in the context of cold atomic gases in optical lattices. Interestingly, it has also been recently observed in magic angle graphene [137]. In the present model, the large entropy of the insulating phase due to frustration and competing orders is responsible for this effect.

An important aspect of the thermodynamics is the behavior of the specific heat at low temperatures. In particular, the behavior of the specific heat allows us to distinguish between gapped and gapless phases. Here, we investigate the internal energy E instead of the specific heat $C = \partial E/\partial T$, since we measure the energy directly, whereas the specific heat is obtained from a numerical derivative of the energy. Our results for $U/t = 8, 10, 12$ are shown in Fig. 5(c). An analysis of the convergence as a function of bond dimension for $U/t = 10$ is shown in the appendix in Fig. 9. In the case of $U/t = 8$, we find that the internal energy E approximately behaves as $E \propto T^2$ for temperatures $0.02 \leq T/t \leq 0.1$, which is indicated by the black dashed lines. This translates to a T -linear behavior of the specific heat upon differentiation. Similarly, for $U/t = 10$ and $U/t = 12$ the energy is well-described by $E \propto T^2$ behavior for $0.0125 \leq T/t \leq 0.4$. We notice, that the temperatures in this regime coincide with region below the peak in the specific heat in Fig. 5(a). For comparison, we also show a scaling $E \propto T^{5/3}$ (i.e. $C \propto T^{2/3}$) as a gray dotted line, which is the expected behavior of a spinon Fermi surface state [68–70]. As can be seen in Fig. 5(c) our data is in closer agreement to a $E \propto T^2$ than the $E \propto T^{5/3}$ scenario. The T -linear behavior we observe would indicate a gapless state. However, we would like to point out that the lowest temperature attained in these simulations is $T/t = 0.0125$. Hence, our data does not rule out an activated behavior from a gap smaller than this temperature. We would like to point out, that these results are in agreement with experimental measurements of the specific heat for the triangular lattice compound κ -(ET)₂Cu₂(CN)₃ [138].

V. MAGNETISM

We study the magnetic properties as a function of temperature and interaction strength of the system on the YC4 cylinder using the METTS algorithm. Results on magnetic ordering from (dynamical) mean-field theory can be found in Appendix C. To distinguish different kinds of orderings, we investigate the magnetic structure factor,

$$S_m(\mathbf{k}) = \frac{1}{N} \sum_{l,m=1}^N e^{i\mathbf{k}\cdot(\mathbf{r}_l - \mathbf{r}_m)} \langle \vec{S}_l \cdot \vec{S}_m \rangle. \quad (16)$$

The momenta \mathbf{k} resolved by the YC4 cylindrical geometry are shown in the inset of Fig. 6(a). Magnetic 120° Néel order can be detected by observing a peak in the structure factor at the K point in the Brillouin zone. On the YC4 cylinder, the K point is not exactly resolved, which is why we resort to the closest point K' , shown in Fig. 6(a), to indicate 120° Néel order. A peak at the M-point can indicate the following two kinds of magnetic correlations:

- (i) A collinear ‘stripy’ antiferromagnetic ordering is characterized by breaking both spin and discrete C_6

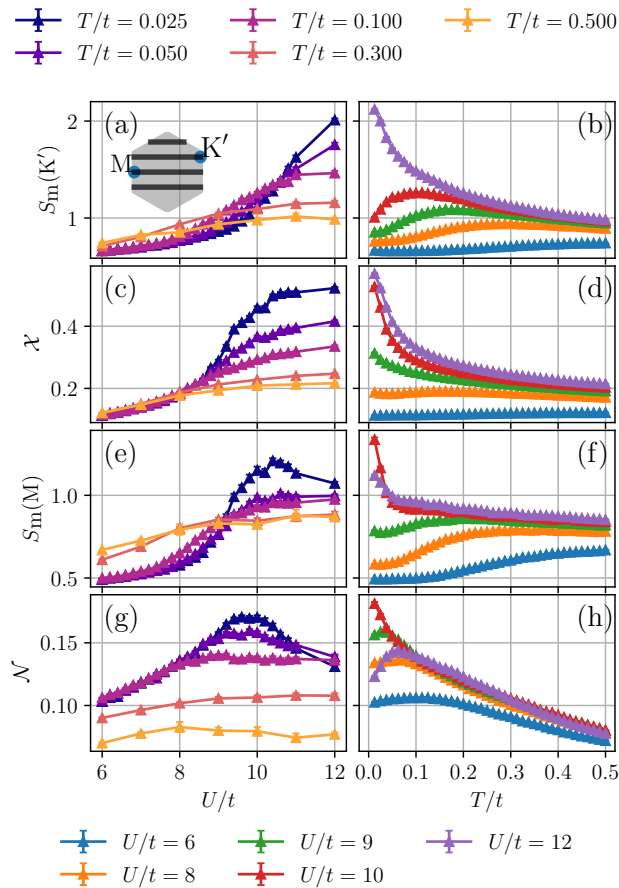


FIG. 6. Magnetic ordering as a function of interaction strength U/t (left) and temperature T/t (right) on the 16×4 YC4 cylinder from METTS. Simulations have been performed with a maximal bond dimension $D_{\max} = 3000$. (a,b) Magnetic structure factor $S_m(K')$ indicating 120° Néel order. The inset in (a) shows the momenta resolved by the YC4 cylinder, and the position of the ordering vectors K' and M (c,d) chiral susceptibility \mathcal{X} as defined in Eq. (17). Chiral correlations build up in both the intermediate as well as the strongly coupled regime at lower temperature. (e,f) Magnetic structure factor $S_m(M)$ indicative of collinear stripy antiferromagnetic order. (g,h) Nematic spin correlation \mathcal{N} , as defined in Eq. (19), is pronounced only in the intermediate coupling regime.

lattice rotation symmetry. This kind of ordering is characterized by the spins being aligned ferromagnetically along one direction of the triangular lattice and antiferromagnetically along the other two. Note that we use here the term ‘stripy’ in relation to spin degrees of freedom - we find no indication of a charge stripe density modulation.

- (ii) Non-coplanar tetrahedral order, on the other hand, is formed when spins in a 2×2 unit cell align in a way that they point towards the corners of a regular tetrahedron [64, 139].

Several recent DMRG studies [52–54] have demonstrated that the triangular Hubbard model in the intermediate regime is susceptible to time-reversal symmetry breaking, which is indicated by a non-zero expectation value of the scalar chirality operator in the thermodynamic limit. To study such a scenario, we compute the chiral susceptibility

$$\mathcal{X} = \frac{1}{N} \sum_{\mu, \nu \in \Delta} \langle \chi_\mu \chi_\nu \rangle, \quad (17)$$

where the scalar chirality operator on a triangle $\mu = (l, m, n)$ is given by

$$\chi_\mu = \vec{S}_l \cdot (\vec{S}_m \times \vec{S}_n). \quad (18)$$

The sum in Eq. (17) extends over all pairs of elementary triangles. In the case of spontaneous time reversal breaking, we expect long range chiral correlations indicated by a large value of the chiral susceptibility \mathcal{X} . Since our simulations are working with real-valued wave functions, the expectation values of the scalar chirality operators, $\langle \chi_\mu \rangle$, are exactly zero.

Moreover, we noticed a particular feature in our data on the YC4 cylinder, where prominent nearest-neighbor antiferromagnetic correlations switch between the different directions of the triangular lattice. To quantify this observation we introduce the nematic spin correlation,

$$\mathcal{N} = -\frac{1}{N} \sum_{\{i, j\}'} \langle \vec{S}_i \cdot \vec{S}_j \rangle, \quad (19)$$

where the sum extends only over nearest-neighbor pairs $\{i, j\}'$ along the short direction of the cylinder (i.e. the direction pointing “north-east” in Fig. 7). The behavior of the above quantities as both a function of U/t and temperature T/t is shown in Fig. 6. We observe three distinct regimes as a function of U/t . For $U/t \lesssim 8.5$ we do not observe any dominant magnetic features. As we have previously found in Fig. 1 and Fig. 2, this region corresponds to the metallic regime.

The intermediate regime ranging from $8.5 \lesssim U/t \lesssim 10.5$ exhibits interesting and peculiar behavior in all observables. With decreasing temperature, magnetic correlations grow as signaled by the structure factor at both the K' and M points Fig. 6(b,f). But below the temperature $T/t = 0.1$ for $U/t = 10$, the K' -point structure factor begins to decrease, while at the M -point it increases sharply beginning around $T/t = 0.05$. The chiral correlations in Fig. 6(d) also increase below this scale, and the specific heat simultaneously develops a small maximum then rapidly decreases as shown in Fig. 5(a). The development of low-T chiral correlations is consistent with previous DMRG results [52, 54], which proposed that at $T = 0$ the system spontaneously breaks time-reversal symmetry and forms a chiral spin liquids. However, we also observe that the chiral correlations similarly build up beyond $U/t \gtrsim 10.5$.

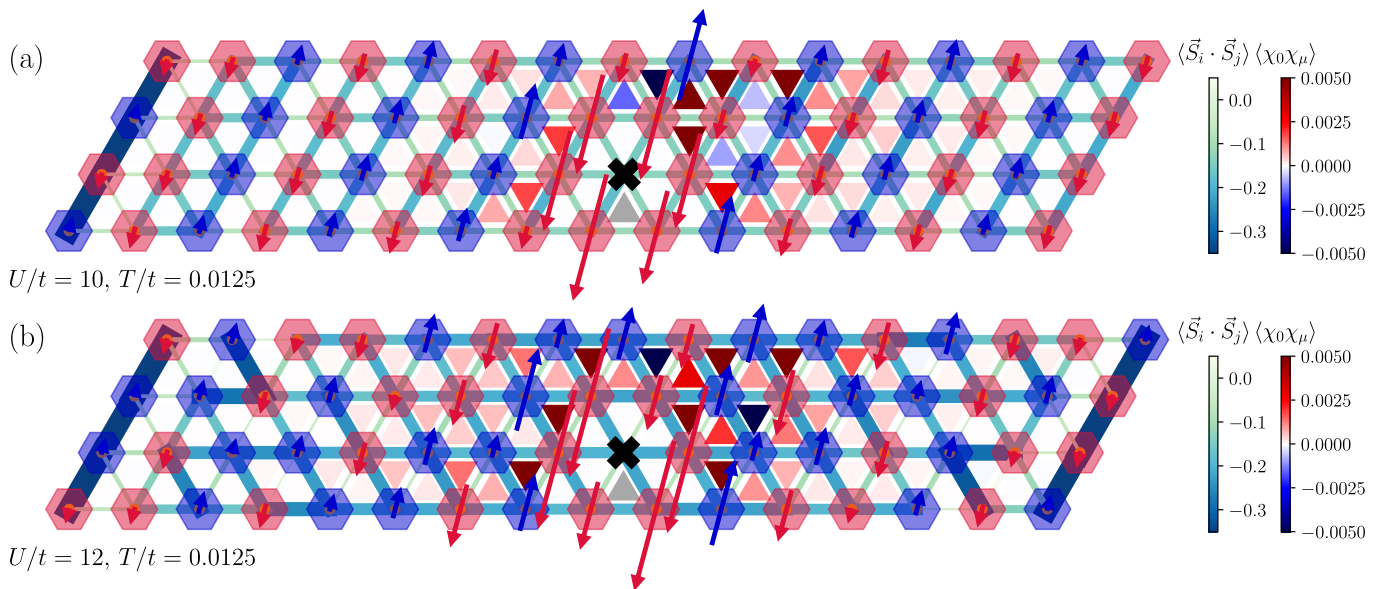


FIG. 7. Snapshots of METTS states $|\psi_i\rangle$ at temperature $T/t = 0.0125$ on the 16×4 YC4 cylinder in the intermediate regime at $U/t = 10$ (a) and in the strong coupling regime at $U/t = 12$ (b). The length of the arrows is proportional to the spin correlation $\langle \vec{S}_0 \cdot \vec{S}_i \rangle$, where the black cross marks the reference site. Hexagons and arrows which are blue indicate positive and red indicate negative spin correlations. The color of the triangles indicates the magnitude of the chiral correlation $\langle \chi_0 \chi_\mu \rangle$, where the reference triangle is indicated in gray just below the reference site. Nearest-neighbor spin correlations $\langle \vec{S}_i \cdot \vec{S}_j \rangle$ are indicated as the width and color of the bonds. We observe collinear stripy spin correlations at this temperature in the intermediate regime at $U/t = 10$.

As already pointed out before, in principle a peak at the M point in the intermediate regime could also indicate non-coplanar tetrahedral magnetic order [139]. However, by inspecting real space spin correlations we clearly observe the formation of stripy antiferromagnetism. Using METTS we can investigate “snapshots” of the system at a given temperature [99]. Briefly summarized, the METTS method decomposes the thermal density matrix into a sum over rank-1 density matrices corresponding to pure states [83, 84],

$$\frac{1}{\mathcal{Z}} e^{-\beta H} = \sum_i p_i |\psi_i\rangle \langle \psi_i|, \quad (20)$$

where $p_i \geq 0$ are real non-negative probabilities, $|\psi_i\rangle$ are the so-called METTS wave functions, and \mathcal{Z} denotes the partition function. The pure states $|\psi_i\rangle$ are sampled with probability p_i . We show the properties of a typical METTS wave function sampled in our simulations at $T/t = 0.0125$ and $U/t = 10$ in Fig. 7(a). The stripy spin correlations are clearly pronounced for this METTS state. We also observe sizeable chiral correlations $\langle \chi_0 \chi_\mu \rangle$ which are indicated by the color of the inner triangles. When comparing the snapshot at $U/t = 10$ in Fig. 7(a) to the snapshot at a larger $U/t = 12$ in Fig. 7(b) we observe that the nearest-neighbor spin correlations are more strongly pronounced along the short direction of the cylinder at $U/t = 10$, whereas for $U/t = 12$ the spin correlations on the other two directions are enhanced.

This motivates the definition of the nematic spin cor-

relation \mathcal{N} in Eq. (19). In Fig. 6(g,h) we observe that \mathcal{N} is clearly pronounced only in the intermediate regime. We would like to point out that the increased magnetic correlations align with the stripy spin patterns, as can be seen in Fig. 7(a).

One last notable aspect of the intermediate regime we find is that increasing the temperature from $T = 0$ not only suppresses double occupancy, as shown previously in Fig. 5, but also increases the 120° Néel order correlations. Therefore, the effect of increasing temperature is similar to the effect of further increasing the coupling strength U/t , which also both localizes the system and favors 120° Néel order for $U/t \geq 10.5$.

The strong coupling regime $U/t \gtrsim 10.5$ is most prominently characterized by the increase in the magnetic structure factor $S_m(\mathbf{K}')$ at lower temperatures, shown in Fig. 6(a,b). This is indicative of 120° Néel order in the ground state. We observe strong antiferromagnetic correlations for $U/t = 12$ setting in at a temperature below $T/t = 0.05$, which again coincides with the small maximum in the specific heat observed in Fig. 5(a). We find that the behavior of the chiral correlations is similar to the intermediate coupling regime. In particular, \mathcal{X} as shown in Fig. 5(d) is rather comparable between $U/t = 10$ and $U/t = 12$.

VI. DISCUSSION

The physics of the triangular lattice Hubbard model at half-filling is coarsely organized in three different regimes as a function of the coupling strength, U/t : a metallic regime is followed by an intriguing insulating regime at intermediate coupling regime whose nature is currently hotly debated. At large interaction strength the system enters a magnetic insulating regime, where coplanar 120° Néel order is stabilized in the ground state. Evidence for the existence of an intermediate non-magnetic insulating regime is ample in the literature [43, 45–52, 54, 129] and clearly confirmed by several of our findings using multiple numerical methods.

We firmly establish the order-by-disorder effect at intermediate coupling U/t , where increasing temperature paradoxically leads to increased localization, as apparent in the double occupancy shown in Fig. 5(d). As discussed in Sec. IV, this effect is similar to the Pomeranchuk effect [131] observed when liquid Helium 3 solidifies upon heating, and previously found to occur for the Hubbard model in DMFT studies [114, 115, 132, 133, 135]. The decrease in double occupancy upon heating is confirmed by both our METTS and cluster DMFT results, where we found good quantitative agreement between these two very different numerical techniques. This observation suggests that localized excitations carry a large thermal entropy at low temperatures. This is consistent with the Maxwell relation Eq. (15) relating decreasing double occupancy in temperature to an increasing entropy with interaction strength U , which we confirm by computing the thermal entropy from METTS in Fig. 5(b), as also previously observed using the finite-temperature Lanczos method on smaller cluster geometries [130]. Upon increasing the temperature we observe increased 120° Néel correlations for $U/t = 10$ in Fig. 6(b). Hence, both increasing temperature as well as increasing U/t , increase the systems tendency to localize and, therefore, form 120° order. The formation of 120° magnetic order can thus be seen as an analogy of liquid Helium 3 solidifying upon increasing temperature.

This order-by-disorder effect naturally gives rise to the question about the nature of the proliferating excitations causing the localization at finite temperature. Let us first discuss the intermediate coupling regime at $U/t = 10$. As we have shown in Fig. 6, both the chiral correlations as well as the magnetic structure factor at the M point develop a maximum towards $T = 0$ at $U/t = 10$ on the 16×4 YC4 cylinder. Interestingly, finite temperature does not simply melt this ordering. Instead, we observe a maximum in $S_m(K')$ at $T/t = 0.1$ indicating increased 120° spin correlations. It is interesting to note, that increasing temperature appears to have the same effect as increasing interaction strength, which also favors 120° order.

Let us now turn to discussing the orders which may develop in the intermediate regime $8.5 \lesssim U/t \lesssim 10.5$. With decreasing temperature, we find increased chiral

correlations as well as spin correlations at the M point. While the onset of chiral correlations would be consistent with spontaneous time-reversal and parity symmetry breaking, as expected for a ground-state chiral spin liquid (CSL) [52–54], the peak in $S_m(M)$ is not necessarily related to the formation of a CSL. While a peak at the M point could in principle be indicative of non-coplanar tetrahedral order [139], we find that in the present geometry this peak is related to the formation of nematic, stripy antiferromagnetic correlations. This finding is backed up by a recent ground state DMRG study [54], which analogously found a peak in $S_m(M)$ in the intermediate regime, although the authors found these correlations to be only short-ranged at $T = 0$.

The occurrence of stripy spin correlations is remarkable given that most known instances of chiral spin liquids are stabilized in close proximity to non-coplanar magnetically ordered states [57, 59–61, 64, 65]. The melting of non-coplanar magnetic ordering has even been suggested as a guiding principle to understand the formation of CSLs [140]. This seems to be rather different in the present case, where nematic collinear correlations and chiral correlations both develop as the temperature is decreased. In this context, the variational study of the triangular lattice Heisenberg model with an additional ring-exchange term performed in Ref. [71] is particularly interesting. The model with ring exchange can be thought of an approximate low-energy effective Hamiltonian for the intermediate coupling regime [51, 68]. The authors compared variational energies of several Gutzwiller projected ansatz wave functions, including an ansatz for a gapped chiral spin liquid and a gapless nematic spin liquid, breaking rotational symmetry. While both of these wave functions have been shown to have a comparable, competitive energy, the gapless nematic state had the lower variational energy for this particular model. A more recent variational Monte Carlo study has similarly suggested the stabilization of a gapless nematic spin liquid in the context of the half-filled triangular Hubbard model, albeit upon adding further second nearest-neighbor interaction [75]. Remarkably, our finite-temperature METTS simulations now reveal exactly this competition between chiral and stripy spin correlations at finite, but low temperatures. While the recent DMRG studies [52, 54] provided strong evidence, that ultimately at $T = 0$ a CSL is formed on the investigated geometries, we now propose that stripy spin correlations become relevant immediately at finite temperatures. We would like to point out, that an estimate for the gap of the CSL has been stated in Ref. [52] by computing the domain wall tension to be $\Delta \approx 0.0065t$, which is below the lowest temperature $T/t = 0.0125$ we have been able to simulate using METTS on the 16×4 cylinder. It is worth pointing out that the effect of finite-temperatures on the system is non-trivial, as can be seen by the increase in $S_m(K')$ when increasing temperatures in Fig. 6(a), or the decrease of the double occupancy in Fig. 5(d).

This raises the question about whether a (rotationally-

symmetric) perturbation could stabilize nematic stripy (quasi-)order at $T = 0$. In particular, it would be interesting to find out whether indeed a nematic gapless spin liquid with algebraic spin correlations can be realized and to study its transition to the CSL. However, such a state will likely have larger quantum entanglement than the gapped CSL, rendering accurate DMRG computations more difficult.

We expect the balance between chiral or nematic spin correlations to be strongly dependent on the finite size geometry. As the DMRG studies on the YC3-6 and XC4 cylinders have shown [52–54], the precise nature of the ground state still has rather strong dependence on the exact shape of the cylindrical geometry. Therefore, a detailed comparison of our finite-temperature METTS data for different geometries is therefore highly desirable.

We have performed an in-depth comparison between different geometries in appendix B. There, we discuss results on YC4 cylinders of varying length and also results on the YC3 and XC4 cylinders [52]. We find that our results only weakly depend on the length of the YC4 cylinders. The specific heat of the YC4 cylinder closely resembles the specific heat obtained on the YC3 and XC4 cylinders. In particular, we observe that the maxima for different values of U/t develop at comparable temperatures across all different geometries. Similarly, the Pomeranchuk effect of decreasing double occupancy as a function of temperature is clearly observed on all geometries. The correlations at low temperatures in the intermediate coupling regime differ, however. While both the YC4 and YC3 geometries exhibit pronounced stripy antiferromagnetic correlations, this is not observed on the XC4 cylinder. Also, the chiral susceptibility only smoothly increases as a function of U/t on the YC3 and XC4 cylinders. This is in contrast to the YC4 cylinder, where we observe the onset of chiral correlations at smaller U/t than the onset of 120° magnetic correlations.

At this point, we would like to comment that finite-size effects are expected to become less severe at higher temperatures, since correlation lengths typically decrease. It remains to be seen down to which temperature scale the finite-size cylinders can fully capture the two-dimensional limit.

Let us now focus on the strong coupling regime at $U/t = 12$. In the limit $U/t \rightarrow \infty$ the effective spin degrees of freedom are described by the antiferromagnetic Heisenberg model, whose 120° Néel ordered ground state features spin-wave excitations. However, besides spin-wave excitations several authors have found a different kind of excitation being relevant in this case. Series expansions found anomalous behavior of the magnon spectrum, which exhibits a minimum beyond the description of linear spin-wave theory [141–143]. This minimum is ascribed to the presence of a different kind of excitations, reminiscent of the roton excitations of ^4He forming a minimum in the quasiparticle dispersion [144, 145]. Therefore, the excitations of the triangular lattice Heisenberg antiferromagnet have often been referred to in literature

as “rotonlike” excitations (RLE). It has been argued that these excitations contribute significantly to the thermal entropy down to temperatures $T \approx 0.1J$ [142], where J denotes the antiferromagnetic coupling constant. More thoroughly, the presence of two different kinds of excitations in the $S = 1/2$ triangular Heisenberg antiferromagnet has been recently using the exponential tensor renormalization group (XTRG) method [146, 147], which similar to METTS, allows for unbiased numerical simulations at finite-temperature on cylindrical geometries. The authors indeed establish two temperature scales corresponding to the magnon and the RLEs. The RLEs are shown to manifest themselves in an increase of the nearest-neighbor chiral correlations as well as a maximum in the magnetic structure factor $S_m(\mathbf{M})$ [147]. The existence of the RLEs is demonstrated to be robust on a wide variety of cylinder geometries, including cylinders of circumference $W = 6$.

In our simulations at $U/t = 12$ we analogously find a maximum in $S_m(\mathbf{M})$ in Fig. 6(e) indicating the RLEs. Also an increase of chiral correlations in Fig. 6(d) at temperatures below $T/t \approx 0.1$ is observed. The 120° magnetic correlations at lower temperatures are signalled by a peak in $S_m(\mathbf{K}')$. This clearly resembles the situation encountered in the Heisenberg model as in Ref. [147]. Interestingly, we found the specific heat in Fig. 5 to be rather similar for both the intermediate and strong coupling regime. It appears that tuning the interaction strength from $U/t = 10$ to $U/t = 12$ interchanges the role of stripy correlations with 120° correlations.

We would like to elaborate on the behavior of the chiral susceptibility \mathcal{X} . If time-reversal symmetry is indeed broken at low-temperature in the intermediate regime, we would expect the chiral correlations to diverge towards $T = 0$. However, we think that the temperatures ($T \geq 0.0125t$) we simulated are above the transition temperature estimated by Ref. [52], $\Delta \approx 0.0065t$. Furthermore, it has also been argued that the stabilization of a CSL at $T = 0$ can depend on the cylinder length studied in DMRG [54], where a CSL at $T = 0$ has only been found in cylinders of length $L = 64$, but not in shorter cylinders. Nevertheless, we find pronounced chiral correlations in the intermediate coupling regime. For the strong coupling regime, pronounced chiral correlations at finite-temperature have been found in a previous study of the Heisenberg model using XTRG [147]. There, the correlations have been attributed to the rotonlike excitations of the triangular lattice Heisenberg antiferromagnet. Here, we find that the chiral correlations already build up in the intermediate regime and remain sizeable in the strong coupling regime. This strongly suggests that the rotonlike excitations are relevant excitations in the intermediate coupling regime.

Finally, an outstanding question is the occurrence of superconductivity in the present model. While general arguments suggest that the metallic phase studied here hosts a low-temperature superconducting instability at weak coupling (see e.g. [148]), the possible occurrence

of an unconventional superconducting phase near the metal-insulator phase boundary [45] or upon doping the insulating phase [67] are intriguing questions for future computational studies.

ACKNOWLEDGEMENTS

We are indebted to Nils Wentzell, Steven White, Michael Zaletel, and Sabine Andergassen for insightful discussions and support. We thank Elio König for valuable comments on the manuscript. We thank the computer service facility of the MPI-FKF, and the Scientific Computing Core of the Flatiron Institute for their help. METTS results were obtained using the ITensor Library (C++ version) [149] and CDMFT computations used the TRIQS library [150]. This work was granted access to the HPC resources of TGCC and IDRIS under the allocations A0090510609 attributed by GENCI (Grand Equipement National de Calcul Intensif). The authors gratefully acknowledge use of the computational resources of the Max Planck Computing and Data Facility. The present work was supported by the Austrian Science Fund (FWF) through the Erwin-Schrödinger Fellowship J 4266 - “Superconductivity in the vicinity of Mott insulators” (SuMo, T.S.). It also has been supported by the Simons Foundation within the Many Electron Collaboration framework. A.G. also acknowledges the support of the European Research Council (ERC-QMAC-319286). The Flatiron Institute is a division of the Simons Foundation.

APPENDIX

Appendix A: Convergence of METTS simulations

We employ the METTS algorithm as described in Ref. [99]. Thermal expectation values of an operator \mathcal{O} are evaluated as,

$$\langle \mathcal{O} \rangle = \overline{\langle \psi_i | \mathcal{O} | \psi_i \rangle}, \quad (\text{A1})$$

where the minimally-entangled typical thermal states,

$$|\psi_i\rangle = e^{-\beta H/2} |\sigma_i\rangle, \quad (\text{A2})$$

are imaginary-time evolved product states $|\sigma_i\rangle$. Here, $\overline{\dots}$ denotes statistical averaging over a series of subsequent METTS. As such, the METTS algorithm is subject to statistical sampling uncertainty, which can be reduced by computing more samples and whose size can be estimated using standard time series analysis. The imaginary-time evolution is performed by using the time-dependent variational principle (TDVP) algorithm for matrix product states [151–153]. In Ref. [99], some of us showed that the maximal bond dimension d of the matrix product state representation of the METTS serves as a control

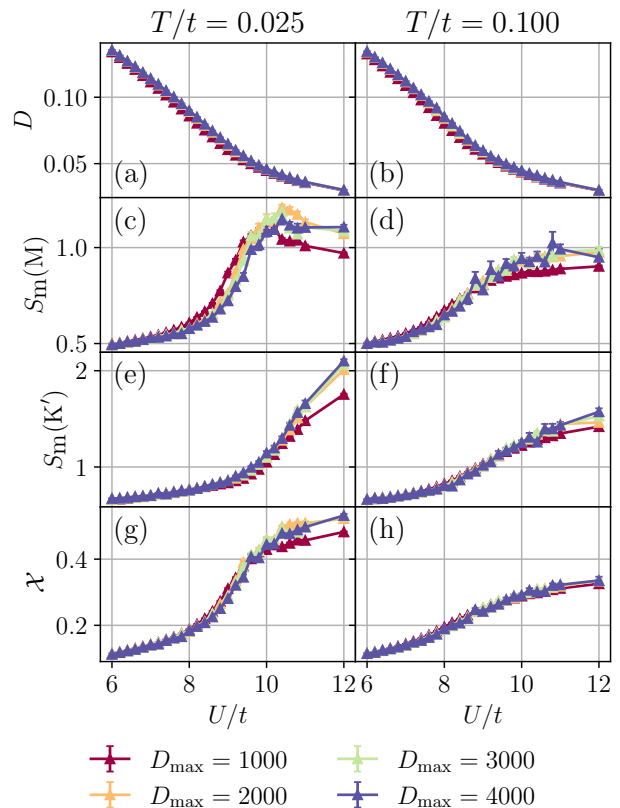


FIG. 8. Convergence of METTS results on the 16×4 YC4 cylinder as a function of maximal bond dimension D_{\max} . We compare results from simulations performed with $D_{\max} = 1000, 2000, 3000, 4000$. Results agree for all quantities within errorbars for $D_{\max} = 2000, 3000, 4000$, whereas results at $D_{\max} = 1000$ deviate slightly. Comparisons are performed at $T/t = 0.025$ (left) and $T/t = 0.1$ (right). We show the double occupancy D (a,b), the magnetic structure factors evaluated at M (c,d) and K' (e,f), and the chiral susceptibility \mathcal{X} (g,h).

parameter to achieve accurate and controlled computations on finite size cylinders. Here, we performed extensive comparisons between simulations at different bond dimensions. Results on the 16×4 YC4 cylinder at temperatures $T/t = 0.025$ and $T/t = 0.1$ as a function of U/t are shown in Fig. 8. Simulations have been performed up to a maximal bond dimension of $D_{\max} = 4000$. We find that all quantities of interest are converged within errorbars already at $D_{\max} = 2000$.

Furthermore, we have performed an analysis of the effects of finite-bond dimension D_{\max} for our results on the energy E as a function of temperature, as shown in Fig. 9. We find the energy as a function of temperature exhibits $E \propto T^2$ behavior in the regime where $0.0125 \leq T/t \leq 0.4$, which implies that the specific heat C is approximately linear in this regime.

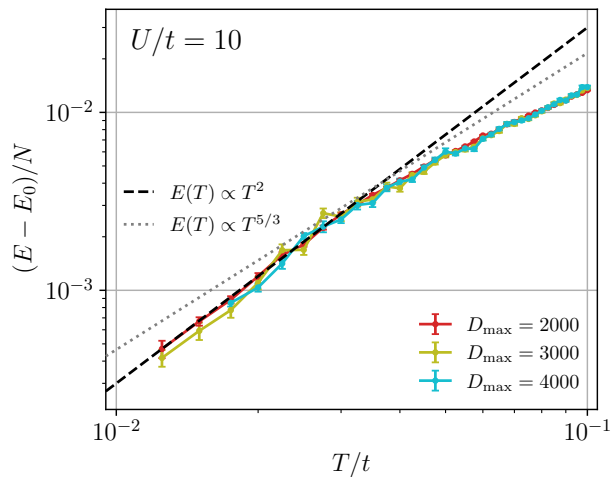


FIG. 9. The internal energy E as a function of T/t at $U/t = 10$ on the 16×4 YC4 cylinder depending on the maximal bond dimension D_{\max} . We compare results from simulations performed with $D_{\max} = 2000, 3000, 4000$ and find our results to agree within errorbars. The behavior of the energy is found to be well described by $E \propto T^2$, implying a T -linear specific heat C .

Appendix B: Comparison of METTS cylinder geometries

The results from METTS in the main text have mainly been obtained on the 16×4 YC4 cylindrical geometry, which is shown in Fig. 7. In this appendix, we discuss the effects of the cylinder geometry on our results. First, we investigate the dependence of the magnetic observables on the cylinder length L of the YC4 cylinder in Fig. 10. We compare simulations at temperatures $T/t = 0.025, 0.100, 0.300$ for $6 \leq U/t \leq 12$. We find that our results only weakly depend on the cylinder length L and are, therefore, expected to be robust in the limit $L \rightarrow \infty$ for the YC4 cylinder.

Moreover, we assess the effect of the cylinder width and boundary conditions on our results. Here, the differences between the geometries are more pronounced, and the physics at lowest temperatures in the intermediate coupling regime differs in some aspects. This has previously already been observed in Refs. [52, 53], where a detailed comparison of DMRG results on different geometries has been performed. We focus on the YC3 and XC4 geometries. The YC3 geometry is similar to the YC4 geometry shown in Fig. 7, but has a circumference of $L_y = 3$. The YC3 geometry allows for stabilizing the 120° Néel order, and features both the K and M points in reciprocal space. The XC4 geometry, on the other hand, has a circumference of $L_y = 4$, but differs from the YC4 geometry by having a distinct periodicity vector given by $T = (0, \frac{\sqrt{3}L_y}{2})$. The 120° Néel order is unfrustrated on this lattice and both K and M points are featured in

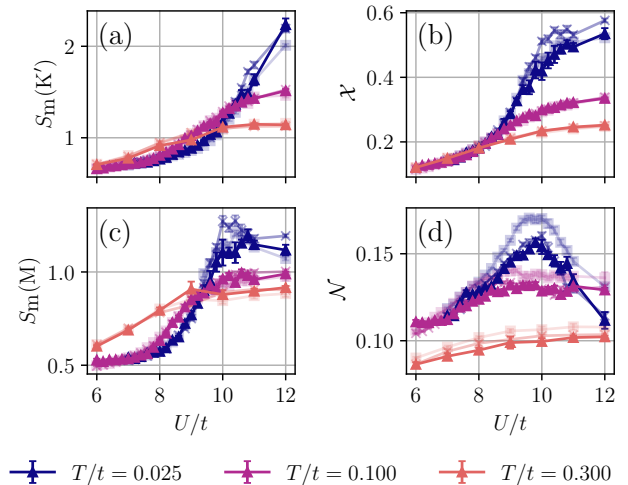


FIG. 10. Size dependence of magnetic structure factor $S_m(\mathbf{k})$ and the chiral susceptibility \mathcal{X} for three different temperatures. We compare YC4 cylinders of length $L = 16$ (squares), $L = 24$ (crosses), and $L = 32$ (triangles). Increasing opacity denotes longer cylinder length. METTS simulations have been performed with a maximal bond dimension $D_{\max} = 4000$ (a) Magnetic structure factor $S_m(K')$ (b) Chiral susceptibility \mathcal{X} (c) Magnetic structure factor $S_m(M)$ (d) Nematic spin correlation \mathcal{N} , from Eq. (19). We observe only weak dependence of these observables on the length L of the cylinder.

reciprocal space. The resolved momenta of the YC3 and XC4 geometry are shown in Fig. 11 and Fig. 12, respectively.

We show the behavior of the specific heat C , magnetic structure factor $S_m(\mathbf{q})$, double occupancy D , and chiral susceptibility \mathcal{X} for the YC3 cylinder in Fig. 11(a) and the XC4 cylinder in Fig. 12(a). First, the behavior of the specific heat is similar on all cylinder geometries we investigated. At $U/t = 6$ we observe a broad maximum at $T/t \approx 0.25 - 0.4$. This maximum is shifted towards lower temperatures of around $T/t \approx 0.15$ at $U/t = 8$. In the intermediate to strong coupling regime, we observe a small maximum at temperatures around $T/t = 0.05$ followed by an extended plateau.

At low temperatures, we observe an increase of the specific heat as a function of U/t , which by Eq. (13) implies an increase in entropy upon increasing U/t . As discussed in Sec. IV, this increase in entropy is related to a decrease of the double occupancy D with temperature via the Maxwell relation Eq. (15). The double occupancy D for the YC3 and XC4 geometries is shown in Fig. 11(c) and Fig. 12(c). The decrease in double occupancy is clearly observed in all geometries. Hence, the Pomeranchuk effect is consistently realized on all geometries we investigated.

The magnetic structure factor $S_m(\mathbf{q})$ at temperature $T/t = 0.025$ as a function of U/t is shown in Fig. 11(b) for the YC3 cylinder and Fig. 12(b) for the XC4 cylinder. The YC3 cylinder exhibits a clearly pronounced

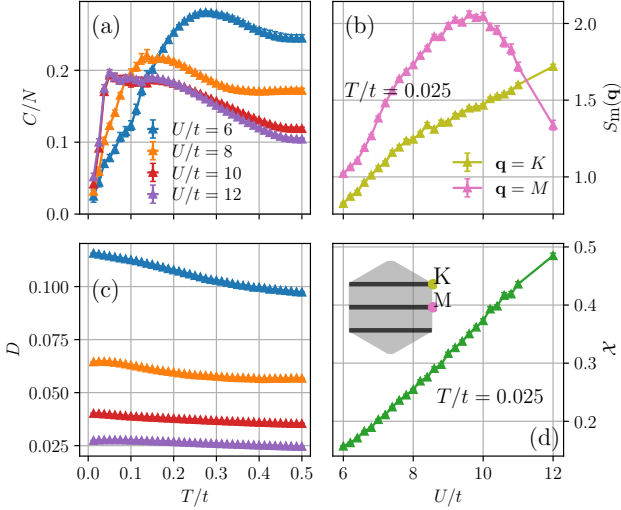


FIG. 11. Key results on the YC3 cylinder from METTS. (a) Specific heat C exhibiting a small peak at $T/t \approx 0.05$ in the intermediate and strong coupling regime. (b) Magnetic structure factor $S_m(\mathbf{q})$ at $T/t = 0.05$ for $\mathbf{q} = M$ and $\mathbf{q} = K$. We observe a peak at $\mathbf{q} = M$ in the intermediate coupling regime. (c) The double occupancy D decreases as a function of temperature. (d) The chiral susceptibility smoothly increases as a function of U/t .

peak at $\mathbf{q} = M$ in the intermediate coupling regime. This is consistent with our results on the YC4 cylinder, where we similarly detected stripy antiferromagnetic order. Also, at strong coupling the structure factor is peaked at $\mathbf{q} = K$, indicating 120° Néel order. However, we do not observe a pronounced chiral susceptibility χ in the intermediate coupling regime in Fig. 11. Instead, the chiral susceptibility smoothly increases as a function of U/t . This is consistent with the ground state DMRG study performed in Ref. [52], where no chiral spin liquid has been observed for periodic boundary conditions on the YC3 cylinder.

Similarly, the XC4 cylinder also does not exhibit a pronounced chiral susceptibility in the intermediate coupling regime in Fig. 12(d). Also for this geometry, Ref. [52] reported the chiral spin liquid not being realized at $T = 0$ for periodic boundary conditions. In contrast to the YC3 and YC4 geometries, the XC4 cylinder does not exhibit a pronounced peak of the magnetic structure factor at the M point in the intermediate regime, as shown in Fig. 12. Instead, the peak at $\mathbf{q} = K$ is smoothly increasing as a function of U/t . This demonstrates that the precise nature of the state realized in the intermediate regime at low-temperatures is dependent on the particular cylinder geometry. We think, the kind of order being exactly realized in the two full-dimensional limit is still to be determined. However, the pronounced the stripy antiferromagnetic correlations on the YC3 and YC4 cylinder and the evidence for a CSL on the YC4 cylinder [52, 54] show that these two kinds of orderings are competing at

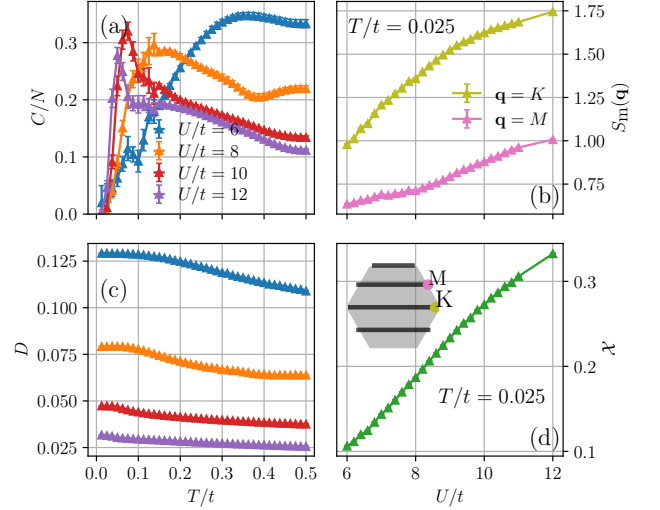


FIG. 12. Key results on the XC4 cylinder from METTS. (a) Specific heat C exhibiting a small peak at $T/t \approx 0.05$ in the intermediate and strong coupling regime. (b) Magnetic structure factor $S_m(\mathbf{q})$ at $T/t = 0.05$ for $\mathbf{q} = M$ and $\mathbf{q} = K$. We do not observe an intermediate peak $\mathbf{q} = M$. (c) The double occupancy D decreases as a function of temperature. (d) The chiral susceptibility smoothly increases as a function of U/t .

the lowest temperatures, and might be realized in the full two-dimensional limit, possibly upon adding further interaction terms.

Appendix C: Magnetic phase transition in (dynamical) mean-field theory

In this Appendix we give an overview of the magnetic properties of the Hubbard model on the isotropic triangular lattice calculated by means of the dynamical mean-field theory (DMFT). By the inclusion of all temporal correlations present in the Hubbard model Eq. (1), DMFT has proven to provide a good starting point for the application of more sophisticated techniques, which aim at including spatial correlations on top (see, e.g., [47, 81, 129, 154]).

The main panel of Fig. 13 shows the Néel temperature calculated in DMFT T_N^{DMFT} (red line and circles) and static mean-field theory (MFT, dashed line), separating the paramagnetic from a magnetically ordered phase [155]. In contrast to the case of the Hubbard model on a square lattice where due to the nesting properties of the Fermi surface the order appears for every finite U at low enough temperatures, here a quantum critical point separates a Fermi liquid from a magnetically ordered ground state at $U_{\text{QCP}}^{\text{DMFT}}/t \approx 9.5$ (cf. also [47, 129]). From there T_N^{DMFT} increases steeply with a maximum of $T_{N,\text{max}}^{\text{DMFT}}/t \approx 0.25$ around $U/t = 11$ before slowly decreasing again.

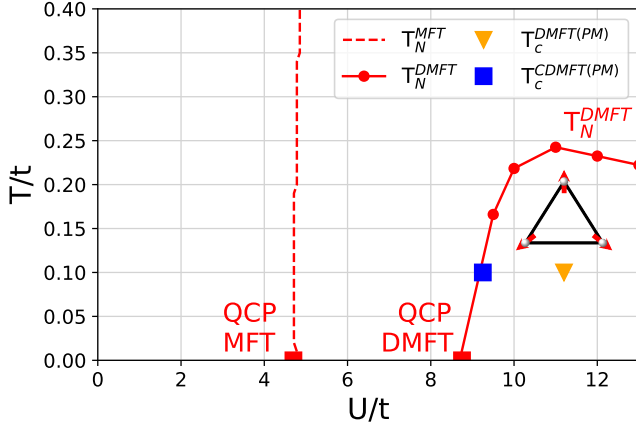


FIG. 13. Magnetic phase diagram of the isotropic triangular Hubbard model calculated by MFT (red dashed line) and DMFT (red circles and solid line). The red lines mark the second order transition from a paramagnet (white) to a 120° Néel ordered phase (red shaded). Also shown are the critical temperatures and interactions of the (PM restricted) DMFT (orange triangle) and CDMFT (blue square). Please note that the CDMFT solution has been restricted to its paramagnetic phase. The DMFT zero temperature point has been taken from the ground state calculation of [113].

Two points are particularly noteworthy:

- (i) as in the case of the Hubbard model on a square lattice the critical end point of the Mott MIT (orange triangle) visible in the paramagnetically restricted DMFT is *shadowed*, i.e. preempted, by the magnetic phase transition of DMFT (with the magnetically order phase being the thermodynamically stable phase of DMFT) and
- (ii) the CDMFT critical end point (blue square) lies close to the phase boundary of the magnetic phase. Please note that we did not calculate the magnetic phase diagram in case of CDMFT, which is restricted to its paramagnetic solution.

Comparing the magnetic phase diagram of DMFT to the self-energies of CDMFT at $T/t = 0.10$ presented in Fig. 4 of the main text, one can observe that the nearest-neighbor component of the CDMFT self-energy starts to increase at the interaction value $U/t = 9.5$, where the DMFT orders magnetically. In other words the spatial mean-field approximation reflects the increase of non-local fluctuations by entering an ordered phase.

For the determination of the DMFT phase boundary, we calculated the momentum-dependent magnetic susceptibility $\chi_m^{\text{DMFT}}(\mathbf{k}, i\Omega_n = 0)$ at zero Matsubara frequency by means of the solution of the Bethe-Salpeter equations with the irreducible vertex extracted from the self-consistently determined Anderson impurity model [93], using the continuous time quantum Monte Carlo solver in its interaction expansion (CT-INT) and the tprf framework [156] of TRIQS [150]. For the vertex we used

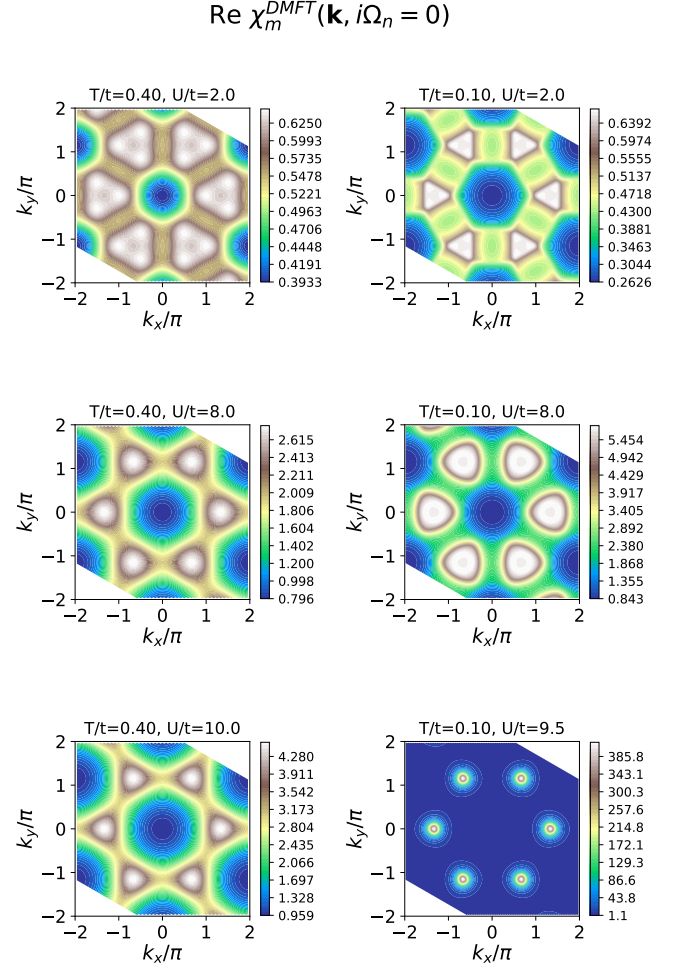


FIG. 14. Momentum dependence of the DMFT magnetic susceptibility at zero frequency for several temperatures and interactions. The leading contribution is (centered around) $\mathbf{k} = K$.

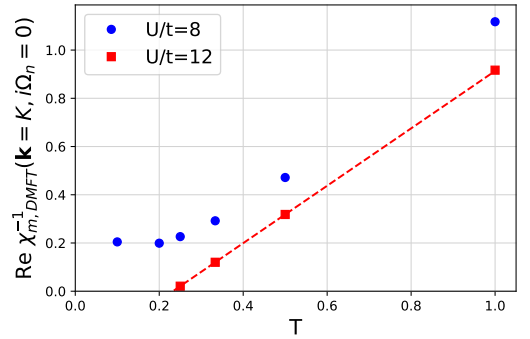


FIG. 15. Temperature dependence of the (inverse) magnetic susceptibility at $\mathbf{k} = K$ and zero Matsubara frequency for two different interaction values calculated by DMFT. For $U/t = 12$ the linear fit to determine T_N^{DMFT} is shown.

up to $N_{i\omega} = 50$ positive fermionic Matsubara frequencies and extrapolated the value of the physical susceptibility

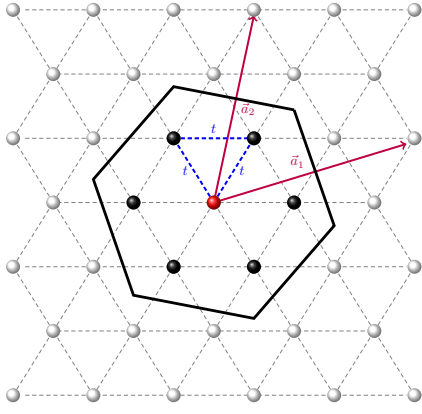


FIG. 16. Cluster geometry with $N_c = 7$ used in CDMFT. The cluster consists of a central site (marked in red) and six equivalent outer sites arranged on a ring. The translation vectors are $\vec{a}_1 = (5/2, \sqrt{3}/2)$ and $\vec{a}_2 = (1/2, 3\sqrt{3}/2)$.

to $N_{i\omega} \rightarrow \infty$ with $\chi \sim a + b/N_{i\omega}$ (see, e.g., Supplemental Material of [157]).

Due to the second order nature of the phase transition, approaching the phase boundary $\chi_m^{\text{DMFT}}(\mathbf{k}, i\Omega_n = 0)$ diverges at the ordering vector $\mathbf{k} = \mathbf{Q}$. Fig. 14 shows $\chi_m^{\text{DMFT}}(\mathbf{k}, i\Omega_n = 0)$ at $T/t = 0.40$ (left column) and $T/t = 0.10$ (right column) for several interaction values. One can see that the leading contribution always stems from momentum vectors centered around $\mathbf{k} = K$. Approaching the transition, at $T/t = 0.10$, $\chi_m^{\text{DMFT}}(\mathbf{k}, i\Omega_n = 0)$ continuously grows before it eventually diverges at $\mathbf{k} = K$. The temperature dependence of the inverse susceptibility $\chi_m^{-1}(\mathbf{k} = K, i\Omega_n = 0)$ is shown in Fig. 15 for two different values of the interaction. At $U/t = 8$ (with a Fermi liquid ground state present in DMFT) it exhibits Pauli-like behavior, i.e. approaching a constant at low temperatures. At $U/t = 10$ (with a magnetically ordered ground state) the susceptibility diverges as $\chi \sim |T - T_N^{\text{DMFT}}|^{-\gamma_T}$ at $T_N^{\text{DMFT}}/t \approx 0.22$ with $\gamma_T = 1$ being the susceptibility's mean-field critical exponent.

Appendix D: Cellular dynamical mean-field theory: cluster geometry, Matsubara data and computational details

a. CDMFT on a $N_c = 7$ site cluster, restricted to the PM solution [CDMFT, CDMFT-7 (PM)]

For the CDMFT calculations performed in this work we used $N_c = 7$ sites which are arranged according to Fig. 16 with a central site and six equivalent sites that form an outer ring. We restrict the CDMFT to its paramagnetic solution. Due to the previously found observation [98] that the self-energy obtained from a cluster center focused extrapolation converges faster with the cluster size than the periodization schemes previously introduced in the literature, for single-particle observables

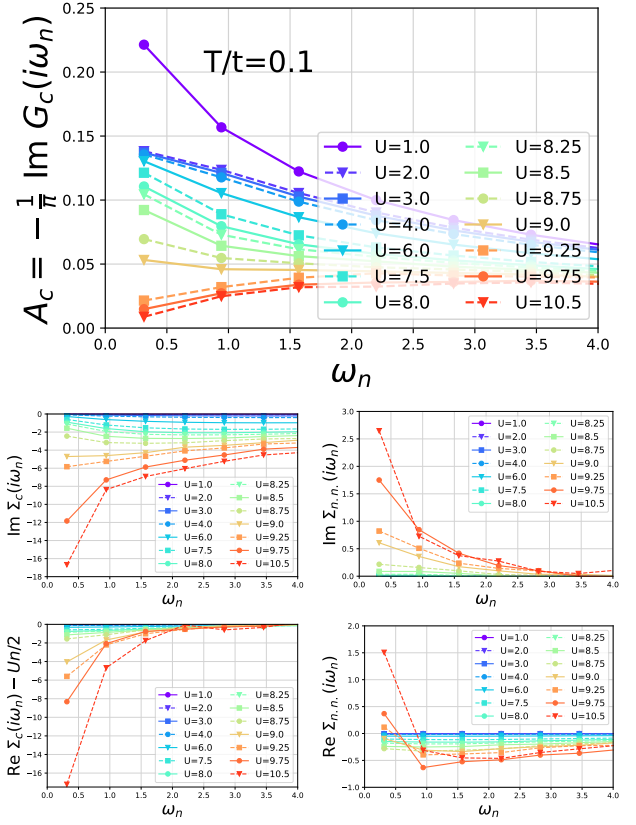


FIG. 17. (Upper row) Spectral weight A_c expressed with the imaginary part of the Green function on the central site of CDMFT at $T/t = 0.1$ for several interaction values as a function of the Matsubara frequency. (Central row) Imaginary part of the self-energy on the central site (left) and to its nearest neighbor (right). (Lower row) Real part of the self-energy on the central site (left, the Hartree term has been subtracted here) and to its nearest neighbor (right).

(like the spectral function shown in panel (a) of Fig. 1) and potential energies (double occupancies) we show values for the central site. Similarly for the self-energies shown in Fig. 4 we took the central site as representative for its local component and as its nearest-neighbor component the values from central site to one of the (equivalent) outer ring sites. This results in a remarkable good agreement with the results from numerically exact DiagMC in the regimes where DiagMC can be controllably resummed.

For completeness and reference in Fig. 17 we show the Matsubara frequency dependence of the single-particle properties spectral function A_c as expressed by the Green function (upper panel), the imaginary part (central panel) and real part (lower panel) of the self-energy. These quantities are shown for $T/t = 0.1$ and for several values of the interaction U/t . For the self-energy we show both the central site and nearest neighbor values. For the real part at the central site we have subtracted the respective Hartree term. The MIT is clearly visible between $U/t = 9$ and 9.25 as (i) a suppression of the spec-

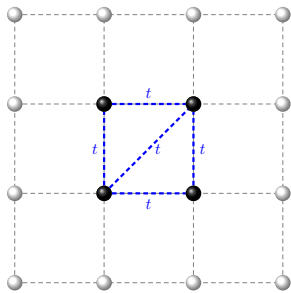


FIG. 18. Cluster geometry with $N_c=4$ used in CDMFT-4.

tral weight at low frequencies and (ii) a change of slope [158, 159]) and eventually divergence of the imaginary part of the self-energy on the central site with increasing U/t . The data of Fig. 1 (a) in the main have been obtained from a linear extrapolation of the data in the upper panel of Fig. 17 to zero frequency.

For the calculations of the self-energies, we converged the CDMFT self-consistency cycle using a continuous time quantum Monte Carlo solver in its interaction expansion (CT-INT) in the TRIQS framework [150].

b. CDMFT on a $N_c=4$ site cluster, allowing for spin-symmetry breaking (CDMFT-4)

For the CDMFT calculations that allow for spin-symmetry breaking (Fig. 3, CDMFT-4) we used a $N_c=4$

cluster with the geometry given in Fig. 18. As already stated in the main text, the convergence of a larger cluster (at least close to phase transitions) is prohibited by the fermionic sign problem.

For being able to enter the symmetry-broken phase we use an approach similar to the one described in [113] for single-site DMFT. However, instead of rotating the Green function we rotate an external magnetic field $H\sigma_z$ by applying:

$$e^{i\phi\sigma_y/2} [H\sigma_z] e^{-i\phi\sigma_y/2} \quad (\text{D1})$$

where $\sigma_i, i \in \{x, y, z\}$ denote the Pauli matrices. The 120° Néel ordering corresponds to a rotation with $\phi = \vec{Q}\vec{R}_i, \vec{Q} = (2\pi/3, 2\pi/3)$. The breaking of the $SU(2)$ -symmetry of the Green function results in an effective 8-orbital calculation at the impurity level. After some iterations of the algorithm we switch off the field and let the system converge self-consistently.

-
- [1] Y. Cao, V. Fatemi, S. Fang, K. Watanabe, T. Taniguchi, E. Kaxiras, and P. Jarillo-Herrero, Unconventional superconductivity in magic-angle graphene superlattices, *Nature* **556**, 43 (2018).
- [2] Y. Cao, V. Fatemi, A. Demir, S. Fang, S. L. Tomarken, J. Y. Luo, J. D. Sanchez-Yamagishi, K. Watanabe, T. Taniguchi, E. Kaxiras, R. C. Ashoori, and P. Jarillo-Herrero, Correlated insulator behaviour at half-filling in magic-angle graphene superlattices, *Nature* **556**, 80 (2018).
- [3] M. Yankowitz, S. Chen, H. Polshyn, Y. Zhang, K. Watanabe, T. Taniguchi, D. Graf, A. F. Young, and C. R. Dean, Tuning superconductivity in twisted bilayer graphene, *Science* **363**, 1059 (2019).
- [4] F. Wu, T. Lovorn, E. Tutuc, and A. H. MacDonald, Hubbard Model Physics in Transition Metal Dichalcogenide Moiré Bands, *Phys. Rev. Lett.* **121**, 026402 (2018).
- [5] F. Wu, T. Lovorn, E. Tutuc, I. Martin, and A. H. MacDonald, Topological Insulators in Twisted Transition Metal Dichalcogenide Homobilayers, *Phys. Rev. Lett.* **122**, 086402 (2019).
- [6] D. M. Kennes, M. Claassen, L. Xian, A. Georges, A. J. Millis, J. Hone, C. R. Dean, D. N. Basov, A. N. Pasupathy, and A. Rubio, Moiré heterostructures as a condensed-matter quantum simulator, *Nat. Phys.* **17**, 155 (2021).
- [7] L. Wang, E.-M. Shih, A. Ghiotto, L. Xian, D. A. Rhodes, C. Tan, M. Claassen, D. M. Kennes, Y. Bai, B. Kim, K. Watanabe, T. Taniguchi, X. Zhu, J. Hone, A. Rubio, A. N. Pasupathy, and C. R. Dean, Correlated electronic phases in twisted bilayer transition metal dichalcogenides, *Nat. Mater.* **19**, 861 (2020).
- [8] Y. Tang, L. Li, T. Li, Y. Xu, S. Liu, K. Barmak, K. Watanabe, T. Taniguchi, A. H. MacDonald, J. Shan, and K. F. Mak, Simulation of Hubbard model physics in WSe_2/WS_2 moiré superlattices, *Nature* **579**, 353 (2020).
- [9] E. C. Regan, D. Wang, C. Jin, M. I. Bakti Utama, B. Gao, X. Wei, S. Zhao, W. Zhao, Z. Zhang, K. Yumigeta, M. Blei, J. D. Carlström, K. Watanabe, T. Taniguchi, S. Tongay, M. Crommie, A. Zettl, and F. Wang, Mott and generalized Wigner crystal states in WSe_2/WS_2 moiré superlattices, *Nature* **579**, 359 (2020), [arXiv:1910.09047 \[cond-mat.mes-hall\]](https://arxiv.org/abs/1910.09047).
- [10] L. An, X. Cai, D. Pei, M. Huang, Z. Wu, Z. Zhou, J. Lin, Z. Ying, Z. Ye, X. Feng, R. Gao, C. Cacho, M. Watson, Y. Chen, and N. Wang, Interaction effects and superconductivity signatures in twisted double-bilayer WSe_2 , *Nanoscale Horiz.* **5**, 1309 (2020).
- [11] L. Xian, D. M. Kennes, N. Tancogne-Dejean, M. Altarelli, and A. Rubio, Multiflat Bands and

- Strong Correlations in Twisted Bilayer Boron Nitride: Doping-Induced Correlated Insulator and Superconductor, *Nano Lett.* **19**, 4934 (2019).
- [12] G. X. Ni, H. Wang, B.-Y. Jiang, L. X. Chen, Y. Du, Z. Y. Sun, M. D. Goldflam, A. J. Frenzel, X. M. Xie, M. M. Fogler, and D. N. Basov, Soliton superlattices in twisted hexagonal boron nitride, *Nat. Commun.* **10**, 4360 (2019).
- [13] K. T. Law and P. A. Lee, 1T-TaS₂ as a quantum spin liquid, *Proceedings of the National Academy of Sciences* **114**, 6996 (2017), <https://www.pnas.org/content/114/27/6996.full.pdf>.
- [14] M. Kratochvilova, A. D. Hillier, A. R. Wildes, L. Wang, S.-W. Cheong, and J.-G. Park, The low-temperature highly correlated quantum phase in the charge-density-wave 1T-TaS₂ compound, *npj Quantum Materials* **2**, 10.1038/s41535-017-0048-1 (2017).
- [15] S. Qiao, X. Li, N. Wang, W. Ruan, C. Ye, P. Cai, Z. Hao, H. Yao, X. Chen, J. Wu, Y. Wang, and Z. Liu, Mottness Collapse in 1T-TaS_{2-x}Se_x Transition-Metal Dichalcogenide: An Interplay between Localized and Itinerant Orbitals, *Phys. Rev. X* **7**, 041054 (2017).
- [16] H. Murayama, Y. Sato, T. Taniguchi, R. Kurihara, X. Z. Xing, W. Huang, S. Kasahara, Y. Kasahara, I. Kimchi, M. Yoshida, Y. Iwasa, Y. Mizukami, T. Shibauchi, M. Konczykowski, and Y. Matsuda, Effect of quenched disorder on the quantum spin liquid state of the triangular-lattice antiferromagnet 1T-TaS₂, *Phys. Rev. Research* **2**, 013099 (2020).
- [17] ET, sometimes also abbreviated as BEDT-TTF, stands for bis(ethylene-dithio) tetrathiafulvalene.
- [18] B. J. Powell and R. H. McKenzie, Quantum frustration in organic Mott insulators: from spin liquids to unconventional superconductors, *Rep. Prog. Phys.* **74**, 056501 (2011).
- [19] K. Kanoda and R. Kato, Mott Physics in Organic Conductors with Triangular Lattices, *Annu. Rev. Condens. Matter Phys.* **2**, 167 (2011).
- [20] T. Furukawa, K. Miyagawa, H. Taniguchi, R. Kato, and K. Kanoda, Quantum criticality of mott transition in organic materials, *Nature Physics* **11**, 221 (2015).
- [21] F. Kagawa, K. Miyagawa, and K. Kanoda, Unconventional critical behaviour in a quasi-two-dimensional organic conductor, *Nature* **436**, 534 (2005).
- [22] T. Komatsu, N. Matsukawa, T. Inoue, and G. Saito, Realization of Superconductivity at Ambient Pressure by Band-Filling Control in κ -(BEDT-TTF)₂Cu₂(CN)₃, *J. Phys. Soc. Jpn.* **65**, 1340 (1996).
- [23] S. Lefebvre, P. Wzietek, S. Brown, C. Bourbonnais, D. Jérôme, C. Mézière, M. Fourmigué, and P. Batail, Mott Transition, Antiferromagnetism, and Unconventional Superconductivity in Layered Organic Superconductors, *Phys. Rev. Lett.* **85**, 5420 (2000).
- [24] P. Limelette, P. Wzietek, S. Florens, A. Georges, T. A. Costi, C. Pasquier, D. Jérôme, C. Mézière, and P. Batail, Mott Transition and Transport Crossovers in the Organic Compound κ -(BEDT-TTF)₂Cu[N(CN)₂]Cl, *Phys. Rev. Lett.* **91**, 016401 (2003).
- [25] Y. Shimizu, K. Miyagawa, K. Kanoda, M. Maesato, and G. Saito, Spin Liquid State in an Organic Mott Insulator with a Triangular Lattice, *Phys. Rev. Lett.* **91**, 107001 (2003).
- [26] Y. Kurosaki, Y. Shimizu, K. Miyagawa, K. Kanoda, and G. Saito, Mott Transition from a Spin Liquid to a Fermi Liquid in the Spin-Frustrated Organic Conductor κ -(ET)₂Cu₂(CN)₃, *Phys. Rev. Lett.* **95**, 177001 (2005).
- [27] S. Ohira, Y. Shimizu, K. Kanoda, and G. Saito, Spin Liquid State in κ -(BEDT-TTF)₂Cu₂(CN)₃ Studied by Muon Spin Relaxation Method, *J. Low Temp. Phys.* **142**, 153 (2006).
- [28] T. Itou, A. Oyamada, S. Maegawa, M. Tamura, and R. Kato, Spin-liquid state in an organic spin-1/2 system on a triangular lattice, EtMe₃Sb[Pd(dmit)₂]₂, *J. Phys. Condens. Matter* **19**, 145247 (2007).
- [29] H. C. Kandpal, I. Opahle, Y.-Z. Zhang, H. O. Jeschke, and R. Valentí, Revision of Model Parameters for κ -Type Charge Transfer Salts: An Ab Initio Study, *Phys. Rev. Lett.* **103**, 067004 (2009).
- [30] S. Maegawa, T. Itou, A. Oyamada, and R. Kato, NMR study of quantum spin liquid and its phase transition in the organic spin-1/2 triangular lattice antiferromagnet EtMe₃Sb[Pd(dmit)₂]₂, *J. Phys. Conf. Ser.* **320**, 012032 (2011).
- [31] T. Isono, H. Kamo, A. Ueda, K. Takahashi, M. Kimata, H. Tajima, S. Tsuchiya, T. Terashima, S. Uji, and H. Mori, Gapless Quantum Spin Liquid in an Organic Spin-1/2 Triangular-Lattice κ -H₃(CAT-EDT-TTF)₂, *Phys. Rev. Lett.* **112**, 177201 (2014).
- [32] E. R. Ylvisaker and W. E. Pickett, First-principles study of the electronic and vibrational properties of LiNbO₂, *Phys. Rev. B* **74**, 075104 (2006).
- [33] K.-W. Lee, J. Kuneš, R. T. Scalettar, and W. E. Pickett, Correlation effects in the triangular lattice single-band system Li_xNbO₂, *Phys. Rev. B* **76**, 144513 (2007).
- [34] T. Soma, K. Yoshimatsu, and A. Ohtomo, p-type transparent superconductivity in a layered oxide, *Sci. Adv.* **6**, 29 (2020).
- [35] J. Hubbard and B. H. Flowers, Electron correlations in narrow energy bands, *Proceedings of the Royal Society of London. Series A. Mathematical and Physical Sciences* **276**, 238 (1963).
- [36] J. Hubbard and B. H. Flowers, Electron correlations in narrow energy bands iii. an improved solution, *Proceedings of the Royal Society of London. Series A. Mathematical and Physical Sciences* **281**, 401 (1964).
- [37] M. C. Gutzwiller, Effect of Correlation on the Ferromagnetism of Transition Metals, *Phys. Rev. Lett.* **10**, 159 (1963).
- [38] J. Kanamori, Electron Correlation and Ferromagnetism of Transition Metals, *Progress of Theoretical Physics* **30**, 275 (1963).
- [39] M. Qin, T. Schäfer, S. Andergassen, P. Corboz, and E. Gull, The Hubbard model: A computational perspective (2021), [arXiv:2104.00064 \[cond-mat.str-el\]](https://arxiv.org/abs/2104.00064).
- [40] D. P. Arovas, E. Berg, S. Kivelson, and S. Raghu, The Hubbard Model (2021), [arXiv:2103.12097 \[cond-mat.str-el\]](https://arxiv.org/abs/2103.12097).
- [41] N. D. Mermin and H. Wagner, Absence of Ferromagnetism or Antiferromagnetism in One- or Two-Dimensional Isotropic Heisenberg Models, *Phys. Rev. Lett.* **17**, 1307 (1966).
- [42] P. C. Hohenberg, Existence of Long-Range Order in One and Two Dimensions, *Phys. Rev.* **158**, 383 (1967).
- [43] H. Morita, S. Watanabe, and M. Imada, Nonmagnetic Insulating States near the Mott Transitions on Lattices with Geometrical Frustration and Implications for κ -(ET)₂Cu₂(CN)₃, *J. Phys. Soc. Jpn.* **71**, 2109 (2002).

- [44] A narrow region of superconductivity has also been suggested using CDMFT between the metal and the non-magnetic insulator [45].
- [45] B. Kyung and A.-M. S. Tremblay, Mott Transition, Antiferromagnetism, and d -Wave Superconductivity in Two-Dimensional Organic Conductors, *Phys. Rev. Lett.* **97**, 046402 (2006).
- [46] P. Sahebsara and D. Sénéchal, Hubbard Model on the Triangular Lattice: Spiral Order and Spin Liquid, *Phys. Rev. Lett.* **100**, 136402 (2008).
- [47] M. Laubach, R. Thomale, C. Platt, W. Hanke, and G. Li, Phase diagram of the Hubbard model on the anisotropic triangular lattice, *Phys. Rev. B* **91**, 245125 (2015).
- [48] K. Misumi, T. Kaneko, and Y. Ohta, Mott transition and magnetism of the triangular-lattice Hubbard model with next-nearest-neighbor hopping, *Phys. Rev. B* **95**, 075124 (2017).
- [49] L. F. Tocchio, F. Becca, A. Parola, and S. Sorella, Role of backflow correlations for the nonmagnetic phase of the t - t' Hubbard model, *Phys. Rev. B* **78**, 041101 (2008).
- [50] T. Yoshioka, A. Koga, and N. Kawakami, Quantum Phase Transitions in the Hubbard Model on a Triangular Lattice, *Phys. Rev. Lett.* **103**, 036401 (2009).
- [51] H.-Y. Yang, A. M. Läuchli, F. Mila, and K. P. Schmidt, Effective Spin Model for the Spin-Liquid Phase of the Hubbard Model on the Triangular Lattice, *Phys. Rev. Lett.* **105**, 267204 (2010).
- [52] A. Szasz, J. Motruk, M. P. Zaletel, and J. E. Moore, Chiral Spin Liquid Phase of the Triangular Lattice Hubbard Model: A Density Matrix Renormalization Group Study, *Phys. Rev. X* **10**, 021042 (2020).
- [53] A. Szasz and J. Motruk, Phase diagram of the anisotropic triangular lattice Hubbard model, *Phys. Rev. B* **103**, 235132 (2021).
- [54] B.-B. Chen, Z. Chen, S.-S. Gong, D. N. Sheng, W. Li, and A. Weichselbaum, Quantum Spin Liquid with Emergent Chiral Order in the Triangular-lattice Hubbard Model (2021), [arXiv:2102.05560](https://arxiv.org/abs/2102.05560).
- [55] V. Kalmeyer and R. B. Laughlin, Equivalence of the resonating-valence-bond and fractional quantum Hall states, *Phys. Rev. Lett.* **59**, 2095 (1987).
- [56] X. G. Wen, F. Wilczek, and A. Zee, Chiral spin states and superconductivity, *Phys. Rev. B* **39**, 11413 (1989).
- [57] L. Messio, B. Bernu, and C. Lhuillier, Kagome Antiferromagnet: A Chiral Topological Spin Liquid?, *Phys. Rev. Lett.* **108**, 207204 (2012).
- [58] r. F. Schroeter, E. Kapit, R. Thomale, and M. Greiter, Spin Hamiltonian for which the Chiral Spin Liquid is the Exact Ground State, *Phys. Rev. Lett.* **99**, 097202 (2007).
- [59] Y.-C. He, D. N. Sheng, and Y. Chen, Chiral Spin Liquid in a Frustrated Anisotropic Kagome Heisenberg Model, *Phys. Rev. Lett.* **112**, 137202 (2014).
- [60] S.-S. Gong, W. Zhu, and D. N. Sheng, Emergent Chiral Spin Liquid: Fractional Quantum Hall Effect in a Kagome Heisenberg Model, *Sci. Rep.* **4**, 6317 (2014).
- [61] A. Wietek, A. Sterdyniak, and A. M. Läuchli, Nature of chiral spin liquids on the kagome lattice, *Phys. Rev. B* **92**, 125122 (2015).
- [62] S. Bieri, L. Messio, B. Bernu, and C. Lhuillier, Gapless chiral spin liquid in a kagome Heisenberg model, *Phys. Rev. B* **92**, 060407 (2015).
- [63] B. Bauer, L. Cincio, B. P. Keller, M. Dolfi, G. Vidal, S. Trebst, and A. W. W. Ludwig, Chiral spin liquid and emergent anyons in a Kagome lattice Mott insulator, *Nat. Commun.* **5**, 5137 (2014).
- [64] A. Wietek and A. M. Läuchli, Chiral spin liquid and quantum criticality in extended $S = \frac{1}{2}$ Heisenberg models on the triangular lattice, *Phys. Rev. B* **95**, 035141 (2017).
- [65] S.-S. Gong, W. Zhu, J.-X. Zhu, D. N. Sheng, and K. Yang, Global phase diagram and quantum spin liquids in a spin- $\frac{1}{2}$ triangular antiferromagnet, *Phys. Rev. B* **96**, 075116 (2017).
- [66] Y.-F. Jiang and H.-C. Jiang, Topological Superconductivity in the Doped Chiral Spin Liquid on the Triangular Lattice, *Phys. Rev. Lett.* **125**, 157002 (2020).
- [67] Z. Zhu, D. N. Sheng, and A. Vishwanath, Doped Mott Insulators in the Triangular Lattice Hubbard Model (2020), [arXiv:2007.11963](https://arxiv.org/abs/2007.11963) [cond-mat.str-el].
- [68] O. I. Motrunich, Variational study of triangular lattice spin-1/2 model with ring exchanges and spin liquid state in κ -(ET)₂Cu₂(CN)₃, *Phys. Rev. B* **72**, 045105 (2005).
- [69] D. N. Sheng, O. I. Motrunich, and M. P. A. Fisher, Spin bose-metal phase in a spin- $\frac{1}{2}$ model with ring exchange on a two-leg triangular strip, *Phys. Rev. B* **79**, 205112 (2009).
- [70] M. S. Block, D. N. Sheng, O. I. Motrunich, and M. P. A. Fisher, Spin bose-metal and valence bond solid phases in a spin-1/2 model with ring exchanges on a four-leg triangular ladder, *Phys. Rev. Lett.* **106**, 157202 (2011).
- [71] T. Grover, N. Trivedi, T. Senthil, and P. A. Lee, Weak Mott insulators on the triangular lattice: Possibility of a gapless nematic quantum spin liquid, *Phys. Rev. B* **81**, 245121 (2010).
- [72] L. F. Tocchio, H. Feldner, F. Becca, R. Valentí, and C. Gros, Spin-liquid versus spiral-order phases in the anisotropic triangular lattice, *Phys. Rev. B* **87**, 035143 (2013).
- [73] R. V. Mishmash, J. R. Garrison, S. Bieri, and C. Xu, Theory of a competitive spin liquid state for weak mott insulators on the triangular lattice, *Phys. Rev. Lett.* **111**, 157203 (2013).
- [74] T. Shirakawa, T. Tohyama, J. Kokalj, S. Sota, and S. Yunoki, Ground-state phase diagram of the triangular lattice Hubbard model by the density-matrix renormalization group method, *Phys. Rev. B* **96**, 205130 (2017).
- [75] L. F. Tocchio, A. Montorsi, and F. Becca, Magnetic and spin-liquid phases in the frustrated t - t' Hubbard model on the triangular lattice, *Phys. Rev. B* **102**, 115150 (2020).
- [76] L. F. Tocchio, A. Montorsi, and F. Becca, The hubbard model on triangular n -leg cylinders: chiral and non-chiral spin liquids (2021), [arXiv:2105.00920](https://arxiv.org/abs/2105.00920).
- [77] C. Peng, Y.-F. Jiang, Y. Wang, and H.-C. Jiang, Gapless spin liquid and pair density wave of the hubbard model on three-leg triangular cylinders (2021), [arXiv:2103.07998](https://arxiv.org/abs/2103.07998).
- [78] J. P. F. LeBlanc, A. E. Antipov, F. Becca, I. W. Bulik, G. K.-L. Chan, C.-M. Chung, Y. Deng, M. Ferrero, T. M. Henderson, C. A. Jiménez-Hoyos, E. Kozik, X.-W. Liu, A. J. Millis, N. V. Prokof'ev, M. Qin, G. E. Scuseria, H. Shi, B. V. Svistunov, L. F. Tocchio, I. S. Tupitsyn, S. R. White, S. Zhang, B.-X. Zheng,

- Z. Zhu, and E. Gull (Simons Collaboration on the Many-Electron Problem), Solutions of the Two-Dimensional Hubbard Model: Benchmarks and Results from a Wide Range of Numerical Algorithms, *Phys. Rev. X* **5**, 041041 (2015).
- [79] B.-X. Zheng, C.-M. Chung, P. Corboz, G. Ehlers, M.-P. Qin, R. M. Noack, H. Shi, S. R. White, S. Zhang, and G. K.-L. Chan, Stripe order in the underdoped region of the two-dimensional Hubbard model, *Science* **358**, 1155 (2017).
- [80] M. Qin, C.-M. Chung, H. Shi, E. Vitali, C. Hubig, U. Schollwöck, S. R. White, and S. Zhang (Simons Collaboration on the Many-Electron Problem), Absence of Superconductivity in the Pure Two-Dimensional Hubbard Model, *Phys. Rev. X* **10**, 031016 (2020).
- [81] T. Schäfer, N. Wentzell, F. Šimkovic, Y.-Y. He, C. Hille, M. Klett, C. J. Eckhardt, B. Arzhang, V. Harkov, F. m. c.-M. Le Régent, A. Kirsch, Y. Wang, A. J. Kim, E. Kozik, E. A. Stepanov, A. Kauch, S. Andergassen, P. Hansmann, D. Rohe, Y. M. Vilc, J. P. F. LeBlanc, S. Zhang, A.-M. S. Tremblay, M. Ferrero, O. Parcollet, and A. Georges, Tracking the Footprints of Spin Fluctuations: A MultiMethod, MultiMessenger Study of the Two-Dimensional Hubbard Model, *Phys. Rev. X* **11**, 011058 (2021).
- [82] J. Kaufmann, K. Steiner, R. T. Scalettar, K. Held, and O. Janson, How correlations change the magnetic structure factor of the kagome Hubbard model (2020), [arXiv:2011.01085 \[cond-mat.str-el\]](https://arxiv.org/abs/2011.01085).
- [83] S. R. White, Minimally Entangled Typical Quantum States at Finite Temperature, *Phys. Rev. Lett.* **102**, 190601 (2009).
- [84] E. M. Stoudenmire and S. R. White, Minimally entangled typical thermal state algorithms, *New J. Phys.* **12**, 055026 (2010).
- [85] N. V. Prokof'ev and B. V. Svistunov, Polaron Problem by Diagrammatic Quantum Monte Carlo, *Phys. Rev. Lett.* **81**, 2514 (1998).
- [86] R. Rossi, Determinant Diagrammatic Monte Carlo Algorithm in the Thermodynamic Limit, *Phys. Rev. Lett.* **119**, 045701 (2017).
- [87] F. Šimkovic and E. Kozik, Determinant Monte Carlo for irreducible Feynman diagrams in the strongly correlated regime, *Phys. Rev. B* **100**, 121102(R) (2019).
- [88] A. Moutenet, W. Wu, and M. Ferrero, Determinant Monte Carlo algorithms for dynamical quantities in fermionic systems, *Phys. Rev. B* **97**, 085117 (2018).
- [89] R. Rossi, F. Šimkovic, and M. Ferrero, Renormalized perturbation theory at large expansion orders, *EPL (Europhysics Letters)* **132**, 11001 (2020).
- [90] F. Šimkovic and R. Rossi, Many-configuration markov-chain monte carlo (2021), [arXiv:2102.05613 \[physics.comp-ph\]](https://arxiv.org/abs/2102.05613).
- [91] W. Metzner and D. Vollhardt, Correlated Lattice Fermions in $d = \infty$ Dimensions, *Phys. Rev. Lett.* **62**, 324 (1989).
- [92] A. Georges and G. Kotliar, Hubbard model in infinite dimensions, *Phys. Rev. B* **45**, 6479 (1992).
- [93] A. Georges, G. Kotliar, W. Krauth, and M. J. Rozenberg, Dynamical mean-field theory of strongly correlated fermion systems and the limit of infinite dimensions, *Rev. Mod. Phys.* **68**, 13 (1996).
- [94] A. N. Rubtsov and A. I. Lichtenstein, Continuous-time quantum monte carlo method for fermions: Beyond auxiliary field framework, *Journal of Experimental and Theoretical Physics Letters* **80**, 61 (2004).
- [95] T. A. Maier, M. Jarrell, T. Pruschke, and M. Hettler, Quantum Cluster Theories, *Rev. Mod. Phys.* **77**, 1027 (2005).
- [96] G. Kotliar, S. Y. Savrasov, G. Pálsson, and G. Biroli, Cellular Dynamical Mean Field Approach to Strongly Correlated Systems, *Phys. Rev. Lett.* **87**, 186401 (2001).
- [97] A. I. Lichtenstein and M. I. Katsnelson, Antiferromagnetism and d-wave superconductivity in cuprates: A cluster dynamical mean-field theory, *Phys. Rev. B* **62**, R9283 (2000).
- [98] M. Klett, N. Wentzell, T. Schäfer, F. Šimkovic, O. Parcollet, S. Andergassen, and P. Hansmann, Real-space cluster dynamical mean-field theory: Center-focused extrapolation on the one- and two particle-levels, *Phys. Rev. Research* **2**, 033476 (2020).
- [99] A. Wietek, Y.-Y. He, S. R. White, A. Georges, and E. M. Stoudenmire, Stripes, antiferromagnetism, and the pseudogap in the doped hubbard model at finite temperature, *Phys. Rev. X* **11**, 031007 (2021).
- [100] M. Troyer and U.-J. Wiese, Computational Complexity and Fundamental Limitations to Fermionic Quantum Monte Carlo Simulations, *Phys. Rev. Lett.* **94**, 170201 (2005).
- [101] F. Šimkovic, M. Ferrero, and R. Rossi, In preparation (2021).
- [102] W. Kohn, Theory of the Insulating State, *Phys. Rev.* **133**, A171 (1964).
- [103] R. Resta and S. Sorella, Electron Localization in the Insulating State, *Phys. Rev. Lett.* **82**, 370 (1999).
- [104] R. Resta, Theory of the insulating state, *La Rivista del Nuovo Cimento* **41**, 463 (2018).
- [105] A. Marrazzo and R. Resta, Local Theory of the Insulating State, *Phys. Rev. Lett.* **122**, 166602 (2019).
- [106] R. Resta, Geometry and topology in many-body physics (2020), [arXiv:2006.15567](https://arxiv.org/abs/2006.15567).
- [107] I. Souza, T. Wilkens, and R. M. Martin, Polarization and localization in insulators: Generating function approach, *Phys. Rev. B* **62**, 1666 (2000).
- [108] R. P. Feynman, Atomic Theory of the Two-Fluid Model of Liquid Helium, *Phys. Rev.* **94**, 262 (1954).
- [109] M. Capello, F. Becca, M. Fabrizio, S. Sorella, and E. Tosatti, Variational Description of Mott Insulators, *Phys. Rev. Lett.* **94**, 026406 (2005).
- [110] L. F. Tocchio, F. Becca, and C. Gros, Backflow correlations in the Hubbard model: An efficient tool for the study of the metal-insulator transition and the large- U limit, *Phys. Rev. B* **83**, 195138 (2011).
- [111] C. De Franco, L. F. Tocchio, and F. Becca, Metal-insulator transitions, superconductivity, and magnetism in the two-band Hubbard model, *Phys. Rev. B* **98**, 075117 (2018).
- [112] S. Li and E. Gull, Magnetic and charge susceptibilities in the half-filled triangular lattice Hubbard model, *Phys. Rev. Research* **2**, 013295 (2020).
- [113] S. Goto, S. Kurihara, and D. Yamamoto, Incommensurate spiral magnetic order on anisotropic triangular lattice: Dynamical mean-field study in a spin-rotating frame, *Phys. Rev. B* **94**, 245145 (2016).
- [114] A. Georges and W. Krauth, Physical properties of the half-filled Hubbard model in infinite dimensions, *Phys. Rev. B* **48**, 7167 (1993).
- [115] M. J. Rozenberg, G. Kotliar, and X. Y. Zhang, Mott-

- hubbard transition in infinite dimensions. ii, *Phys. Rev. B* **49**, 10181 (1994).
- [116] Kotliar, G., Landau theory of the Mott transition in the fully frustrated Hubbard model in infinite dimensions, *Eur. Phys. J. B* **11**, 27 (1999).
- [117] M. J. Rozenberg, R. Chitra, and G. Kotliar, Finite Temperature Mott Transition in the Hubbard Model in Infinite Dimensions, *Phys. Rev. Lett.* **83**, 3498 (1999).
- [118] G. Kotliar, E. Lange, and M. J. Rozenberg, Landau Theory of the Finite Temperature Mott Transition, *Phys. Rev. Lett.* **84**, 5180 (2000).
- [119] R. Bulla, T. A. Costi, and D. Vollhardt, Finite-temperature numerical renormalization group study of the Mott transition, *Phys. Rev. B* **64**, 045103 (2001).
- [120] P. Limelette, Universality and Critical Behavior at the Mott Transition, *Science* **302**, 89 (2003).
- [121] A. Liebsch, H. Ishida, and J. Merino, Mott transition in two-dimensional frustrated compounds, *Phys. Rev. B* **79**, 195108 (2009).
- [122] E. G. C. P. van Loon, F. Krien, and A. A. Katanin, Bethe-Salpeter Equation at the Critical End Point of the Mott Transition, *Phys. Rev. Lett.* **125**, 136402 (2020).
- [123] O. Parcollet, G. Biroli, and G. Kotliar, Cluster Dynamical Mean Field Analysis of the Mott Transition, *Phys. Rev. Lett.* **92**, 226402 (2004).
- [124] H. T. Dang, X. Y. Xu, K.-S. Chen, Z. Y. Meng, and S. Wessel, Mott transition in the triangular lattice Hubbard model: A dynamical cluster approximation study, *Phys. Rev. B* **91**, 155101 (2015).
- [125] H. Lee, G. Li, and H. Monien, Hubbard model on the triangular lattice using dynamical cluster approximation and dual fermion methods, *Phys. Rev. B* **78**, 205117 (2008).
- [126] T. Ohashi, T. Momoi, H. Tsunetsugu, and N. Kawakami, Finite Temperature Mott Transition in Hubbard Model on Anisotropic Triangular Lattice, *Phys. Rev. Lett.* **100**, 076402 (2008).
- [127] P. Sémon and A.-M. S. Tremblay, Importance of sub-leading corrections for the Mott critical point, *Phys. Rev. B* **85**, 201101 (2012).
- [128] A. Vranić, J. Vučićević, J. Kokalj, J. Skolimowski, R. Žitko, J. Mravlje, and D. Tanasković, Charge transport in the Hubbard model at high temperatures: Triangular versus square lattice, *Phys. Rev. B* **102**, 115142 (2020).
- [129] G. Li, A. E. Antipov, A. N. Rubtsov, S. Kirchner, and W. Hanke, Competing phases of the Hubbard model on a triangular lattice: Insights from the entropy, *Phys. Rev. B* **89**, 161118 (2014).
- [130] J. Kokalj and R. H. McKenzie, Thermodynamics of a Bad Metal–Mott Insulator Transition in the Presence of Frustration, *Phys. Rev. Lett.* **110**, 206402 (2013).
- [131] R. C. Richardson, The Pomeranchuk effect, *Rev. Mod. Phys.* **69**, 683 (1997).
- [132] A. Georges and W. Krauth, Numerical solution of the $d=\infty$ hubbard model: Evidence for a mott transition, *Phys. Rev. Lett.* **69**, 1240 (1992).
- [133] A.-M. Daré, L. Raymond, G. Albinet, and A.-M. S. Tremblay, Interaction-induced adiabatic cooling for antiferromagnetism in optical lattices, *Phys. Rev. B* **76**, 064402 (2007).
- [134] A. Georges, Thinking locally: Reflections on Dynamical Mean-Field Theory from a high-temperature/high-energy perspective, *Ann. Phys. (Berl.)* **523**, 672 (2011).
- [135] F. Werner, O. Parcollet, A. Georges, and S. R. Hassan, Interaction-Induced Adiabatic Cooling and Antiferromagnetism of Cold Fermions in Optical Lattices, *Phys. Rev. Lett.* **95**, 056401 (2005).
- [136] S. Taie, R. Yamazaki, S. Sugawa, and Y. Takahashi, An SU(6) Mott insulator of an atomic Fermi gas realized by large-spin Pomeranchuk cooling, *Nature Physics* **8**, 825 (2012), [arXiv:1208.4883](https://arxiv.org/abs/1208.4883) [cond-mat.quant-gas].
- [137] A. Rozen, J. M. Park, U. Zondiner, Y. Cao, D. Rodan-Legrain, T. Taniguchi, K. Watanabe, Y. Oreg, A. Stern, E. Berg, P. Jarillo-Herrero, and S. Ilani, Entropic evidence for a Pomeranchuk effect in magic angle graphene (2020), [arXiv:2009.01836](https://arxiv.org/abs/2009.01836) [cond-mat.mes-hall].
- [138] S. Yamashita, Y. Nakazawa, M. Oguni, Y. Oshima, H. Nojiri, Y. Shimizu, K. Miyagawa, and K. Kanoda, Thermodynamic properties of a spin-1/2 spin-liquid state in a κ -type organic salt, *Nature Physics* **4**, 459 (2008).
- [139] L. Messio, C. Lhuillier, and G. Misguich, Lattice symmetries and regular magnetic orders in classical frustrated antiferromagnets, *Phys. Rev. B* **83**, 184401 (2011).
- [140] C. Hickey, L. Cincio, Z. Papić, and A. Paramekanti, Emergence of chiral spin liquids via quantum melting of noncoplanar magnetic orders, *Phys. Rev. B* **96**, 115115 (2017).
- [141] W. Zheng, J. O. Fjærestad, R. R. P. Singh, R. H. McKenzie, and R. Coldea, Anomalous Excitation Spectra of Frustrated Quantum Antiferromagnets, *Phys. Rev. Lett.* **96**, 057201 (2006).
- [142] W. Zheng, J. O. Fjærestad, R. R. P. Singh, R. H. McKenzie, and R. Coldea, Excitation spectra of the spin- $\frac{1}{2}$ triangular-lattice Heisenberg antiferromagnet, *Phys. Rev. B* **74**, 224420 (2006).
- [143] O. A. Starykh, A. V. Chubukov, and A. G. Abanov, Flat spin-wave dispersion in a triangular antiferromagnet, *Phys. Rev. B* **74**, 180403 (2006).
- [144] L. Landau, Theory of the Superfluidity of Helium II, *Phys. Rev.* **60**, 356 (1941).
- [145] R. P. Feynman, Superfluidity and Superconductivity, *Rev. Mod. Phys.* **29**, 205 (1957).
- [146] B.-B. Chen, L. Chen, Z. Chen, W. Li, and A. Weichselbaum, Exponential thermal tensor network approach for quantum lattice models, *Phys. Rev. X* **8**, 031082 (2018).
- [147] L. Chen, D.-W. Qu, H. Li, B.-B. Chen, S.-S. Gong, J. von Delft, A. Weichselbaum, and W. Li, Two-temperature scales in the triangular-lattice Heisenberg antiferromagnet, *Phys. Rev. B* **99**, 140404 (2019).
- [148] S. Raghu, S. A. Kivelson, and D. J. Scalapino, Superconductivity in the repulsive Hubbard model: An asymptotically exact weak-coupling solution, *Phys. Rev. B* **81**, 224505 (2010).
- [149] M. Fishman, S. R. White, and E. M. Stoudenmire, The ITensor software library for tensor network calculations (2020), [arXiv:2007.14822](https://arxiv.org/abs/2007.14822).
- [150] O. Parcollet, M. Ferrero, T. Ayral, H. Hafermann, I. Krivenko, L. Messio, and P. Seth, TRIQS: A toolbox for research on interacting quantum systems, *Comput. Phys. Commun.* **196**, 398 (2015).
- [151] J. Haegeman, J. I. Cirac, T. J. Osborne, I. Pižorn, H. Verschelde, and F. Verstraete, Time-Dependent Variational Principle for Quantum Lattices, *Phys. Rev. Lett.* **107**, 070601 (2011).

- [152] J. Haegeman, C. Lubich, I. Oseledets, B. Vandereycken, and F. Verstraete, Unifying time evolution and optimization with matrix product states, *Phys. Rev. B* **94**, 165116 (2016).
- [153] S. Paeckel, T. Köhler, A. Swoboda, S. R. Manmana, U. Schollwöck, and C. Hubig, Time-evolution methods for matrix-product states, *Ann. Phys. (N. Y.)* **411**, 167998 (2019).
- [154] S. Li and E. Gull, Magnetic and charge susceptibilities in the half-filled triangular lattice Hubbard model, *Phys. Rev. Research* **2**, 013295 (2020).
- [155] As a spatial mean-field theory, both MFT and DMFT exhibit a second order phase transition (for the exact solution the Mermin-Wagner theorem [41, 42] prohibits magnetic ordering at finite T).
- [156] H. U. R. Strand, N. Wentzell, and O. Parcollet, [tprf - two-particle response function tools based on the TRIQS library](#) (2019).
- [157] T. Schäfer, A. A. Katanin, K. Held, and A. Toschi, Interplay of Correlations and Kohn Anomalies in Three Dimensions: Quantum Criticality with a Twist, *Phys. Rev. Lett.* **119**, 046402 (2017).
- [158] T. Schäfer, F. Geles, D. Rost, G. Rohringer, E. Arrigoni, K. Held, N. Blümer, M. Aichhorn, and A. Toschi, Fate of the false Mott-Hubbard transition in two dimensions, *Phys. Rev. B* **91**, 125109 (2015).
- [159] F. Šimkovic, J. P. F. LeBlanc, A. J. Kim, Y. Deng, N. V. Prokof'ev, B. V. Svistunov, and E. Kozik, Extended Crossover from a Fermi Liquid to a Quasiantiferromagnet in the Half-Filled 2D Hubbard Model, *Phys. Rev. Lett.* **124**, 017003 (2020).